International Journal of Multiphysics
Volume 18, No. 2s, 2024
ISSN: 1750-9548

Multiscale-Multiphysics Model for Optimization of Novel Ceramic MIEC Solid Oxide Fuel Cell Electrodes

Philip Marmet[1,3*], Lorenz Holzer[1], Thomas Hocker[1], Holger Bausinger[2†], Jan G. Grolig[2‡], Andreas Mai[2§], Joseph M. Brader[3] and Gernot K. Boiger[1]

[1.] Zurich University of Applied Sciences, Institute of Computational Physics, 8400, Winterthur, Switzerland

[2.] Hexis AG, CH-8404 Winterthur, Switzerland

[3.] Department of Physics, University of Fribourg, CH-1700 Fribourg, Switzerland

† Present address: Celeroton AG, CH-8604 Volketswil, Switzerland

‡ Present address: Stargate Hydrogen Solutions, Valukoja 8/2, 11415, Tallinn, Estonia

§ Present address: Topsoe Germany GmbH, Alfredstrasse 81, 45130 Essen, Germany

*Corresponding author mame@zhaw.ch

Abstract

To significantly improve on the unavoidable degradation of state-of-the-art Solid oxide fuel cell (SOFC) anodes like Ni-YSZ, we elaborate on fully ceramic composite electrodes, which are based on mixed ionic and electronic conductors (MIEC) like doped ceria and perovskite materials. Thereby, a Digital Materials Design (DMD) framework is used for the systematic and model-based optimization of MIEC SOFC-electrodes. In our DMD approach we combine experimental methods, stochastic microstructure modeling, virtual testing of 3D microstructures and a multiscale-multiphysics electrode model. The electrode model developed in this contribution captures all the relevant physico-chemical processes involved like the transport of charge carriers in the two MIEC solid phases, transport of the gas species in the pore-phase and the reaction kinetics. A special emphasize is laid to the appropriate description of the microstructure effects, applying the previously reported DMD-methodologies. This model-based performance prediction enables to explore a much larger design space than it would be possible with experimental methods only.

1. INTRODUCTION

1.1 Development of novel Ni-free solid oxide cell electrodes

The storage and efficient conversion of energy is one of the key issues for a successful transition to renewable energies. Solid oxide cell (SOC) technology is a promising solution for the conversion of electrical energy to storable chemical energy (power-to-gas) in the solid oxide electrolysis cell (SOEC) mode, and for the on-demand supply of electrical energy using synthetic gas or biogas (or natural gas) as input in the solid oxide fuel cell (SOFC) mode. However, there are still issues especially concerning the degradation behavior and lifetime, which calls for the development of alternative material systems. For example, the most commonly used anode material in SOFCs is Nickel - yttria-stabilized zirconia (Ni-YSZ), which shows various types of degradation [1,2] including Ni coarsening [3], carbon coking [4–6] sulfur poisoning [7] and mechanical damage caused by redox cycling [8]. Moreover, the electrochemical reaction is bound to the three-phase boundaries (TPB), which induces a specific microstructure limitation towards the electrochemical activity in Ni-YSZ cermet anodes. As an alternative anode concept, mixed ionic and electronic conductive (MIEC) materials are drawing much attention. An obvious

advantage of MIEC materials is the fact that the fuel oxidation reaction can take place on the complete MIEC/pore interface (two-phase boundaries). Composite ceramic anodes consisting of perovskite and gadolinium doped ceria (CGO) represent one of the most important alternative material concepts (e.g., [1,9–11]). Thereby, the Ni-phase is replaced by a conductive perovskite-phase (e.g., La, Sr, titanate) with the goal to get rid of the harmful degradation phenomena associated with Ni. CGO provides a high ionic conductivity and a high electrochemical activity, which are both crucial for a high electrode performance. While pure CGO electrodes with a very high performance are possible (e.g., reported by Graves et al. [12] and Nenning et al. [13]), there are issues with the current collection and the structural stability (e.g., nano cracks as reported by Sciazko et al. [1]). In fact, an additional perovskite-phase can provide a structural stabilization effect and thus an improved degradation behavior compared to pure CGO electrodes [1]. In addition, the perovskite introduces an improved current collection functionality because of its high intrinsic electronic conductivity. However, perovskites generally show a lower electrochemical activity compared to CGO. Thus, perovskite-CGO electrodes are often impregnated with an additional nano-sized metal catalyst [11,14–18] in order to improve the electrochemical activity, especially for the case of high perovskite contents.

In the current contribution, a ceramic composite electrode with an LSCT-perovskite phase and a CGO-phase will be studied with an additional Rh-impregnation. However, the anode performance is governed by complex physico-chemical processes including transport of gas species in the pores, transport of ions and electrons in both solid phases and fuel oxidation reaction on the surface of the MIECs, which are not yet fully understood. Hence, there are numerous conflicting requirements and lack of knowledge complicating the development and optimization process. Thus, Digital Materials Design (DMD) methodologies [19],[20] were developed to accelerate the research in this field in a cost-efficient way. In our DMD approach we combine experimental methods, stochastic microstructure modeling, virtual testing of 3D microstructures and a multiscale-multiphysics electrode model. While the modules of this DMD-methodologies for stochastic microstructure modelling (Marmet et al. [20], [21]) and standardized microstructure characterization (Marmet et al. [22], [23]) are already published, the multiscale-multiphysics electrode model will be reported in this contribution (section 3). Moreover, the whole DMD-workflow is illustrated for the optimization of LSCT-CGO electrodes. Therefore, also two sets of experimental data will be used, namely 1) FIB-SEM tomography to fit the stochastic microstructure model and 2) performance characterization of the cells by electrochemical impedance spectroscopy (EIS) to calibrate the reaction kinetics within the multiphysics electrode model.

1.2. Important properties of LSCT-CGO MIEC electrodes

The use of a ceramic composite with two MIEC phases for an SOFC anode results in complex physico-chemical processes involved governing the anode performance. Thus, additional aspects need to be considered for the microstructure and cell design, which are quite different compared to the conventional SOFC anodes like Ni-YSZ. The physico-chemical phenomena involved in LSCT-CGO electrodes and the corresponding microstructure properties are illustrated in Fig. 1.

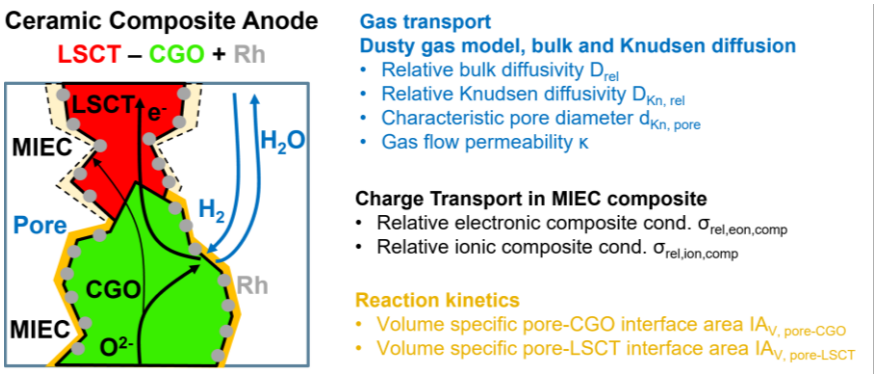

Fig. 1: Illustration of the main physical phenomena and associated microstructure effects present in an LSCT-CGO anode with Rh impregnation. On the right side, the effective transport properties and microstructure characteristics are listed, which are used as input for the multiphysics model. The color code of the list corresponds with the one in the figure.

The gas transport within the pores of an SOC electrode is governed by diffusion. However, for fine porous microstructures with pores in the range of sub-microns, the transport is governed by bulk and Knudsen diffusion. The latter describes scattering events of gas molecules at the pore walls. Fine porous microstructures are relevant for electrode optimization because of their potentially high electrochemically activity associated with their high volume specific surface area or TPB-length. To capture the Knudsen effects in fine structured electrodes, the well-known dusty-gas model (DGM) is often used to describe the combined transport mechanism by bulk and Knudsen diffusion appropriately [24–27]. An implementation and further description of the dusty-gas model can be found in Marmet et al. [28]. For the parametrization of the dusty-gas model, four microstructure properties are needed: the relative bulk diffusivity D_{rel} (Eq. 17), the relative Knudsen diffusivity $D_{\mathrm{rel,Kn}}$ (Eq. 18), the characteristic Knudsen length $d_{\mathrm{Kn,pore}}$ and the gas permeability κ.

A unique feature for composite MIEC electrodes like LSCT-CGO is revealed with a remarkable property that can be described as 'composite conductivity'. Due to the fact that both solid phases are mixed ion- and electron-conductors, the transports of neither the electrons nor the oxygen ions are limited to a single phase. However, the intrinsic conductivities are different, i.e., the intrinsic ionic conductivity of CGO is about ten times higher than for LSCT and the intrinsic electronic conductivity of LSCT is about ten times higher than for CGO. Nevertheless, the effective ionic composite conductivity $\sigma_{\mathrm{eff,ion,comp}}$ (Eq. 7) and the effective electronic composite conductivity $\sigma_{\mathrm{eff,eon,comp}}$ (Eq. 8) are much higher than the (hypothetical) single-phase conductivities of the same microstructure. In composite MIEC anodes, the charge carriers can reach the reaction sites even when the volume fraction of one MIEC-phase is below the percolation threshold. These MIEC properties thus open a much larger design space for microstructure optimization of ceramic composite electrodes.

As a consequence of the composite with two MIEC materials, the possible reaction sites, e.g., for the hydrogen oxidation reaction (HOR), are extended to the entire pore-CGO and pore-LSCT interface area. Thus, the volume specific pore-CGO $IA_{\mathrm{V,pore\text{-}CGO}}$ and pore-LSCT $IA_{\mathrm{V,pore\text{-}LSCT}}$ interface areas are the relevant microstructure properties for the reaction kinetics. Thereby, the reaction kinetics are improved by the impregnated Rh particles. The reaction kinetics of this material system needs to be calibrated to corresponding electrochemical performance characterizations, as reported in section 3.3.2.

2. MATERIALS AND METHODS

2.1 Experimental

2.1.1. Fabrication of the LSCT-CGO+Rh cells

A batch of button cells was fabricated in order to study the microstructure and performance of LSCT-CGO anodes with different compositions. The LSCT ($\mathrm{La_{0.20}Sr_{0.25}Ca_{0.45}TiO_3}$) was supplied by Praxair Surface Technologies Inc. and the CGO was supplied by Solvay. The button cells were fabricated by screen printing (using a manual process) the anode and the cathode layers onto a 160 µm thick electrolyte disk from 6ScSZ (HEXIS). The button cells were prepared as full cells with an electrolyte supported cell design with an active area of $1.44\mathrm{cm}^2$. Both, the LSCT-CGO anode layer and the double layered LSM-based cathode were prepared using the previously reported preparatory methods [11,29,30]. For the anode, separate slurries were prepared for CGO and the LSCT, which were then mixed to achieve the different compositions. After the sintering process, the anode was impregnated with an Rh-solution using a pipette, resulting in a Rh-loading in the range of $\leq 1\mathrm{wt.\%}$. Rh belongs to one of the suitable metal catalysts for the impregnation of SOFC anodes tested by Price et al. [11] (like Ni, Pd, Pt, Rh and Ru) in order to improve the reaction kinetics. The anode side was contacted with a porous Ni current collector layer (CCL) and with a Ni-mesh and the cathode side with a gold-mesh.

2.1.2 FIB-SEM tomography

Five 3D microstructures with different LSCT:CGO compositions have been reconstructed using FIB-SEM tomography including a 100 % CGO (CGO100) and a 100 % LSCT (LSCT100) sample. The image acquisition

and segmentation have been performed according to the procedure reported in Marmet et al. [22]. An overview of the microstructures is presented in the top row of Fig. 3.

2.1.3 Electrochemical impedance spectroscopy

The button cells (full cells) are operated on a seal-less button cell test stand at the laboratories of HEXIS with a post-cell combustion zone. A more detailed description of the test stand can be found in the work of Price et al. [11]. For the EIS-measurements a Zennium PP241 from Zahner is used. An excess hydrogen fuel supply on the anode side and an excess compressed air supply on the cathode side are used in order to avoid gas conversion impedance effects. The OCV and therewith the water content of the fuel is varied by changing the fuel flowrate, which results in a specific gas composition due to the leakage of the seal-less setup. A fixed air flowrate of 520 ml/min is used on the cathode side. A more detailed description of the measurement setup can be found in the PhD-thesis of Ph. Marmet [19].

2.2 Digital Materials Design: Modeling methods

2.2.1. DMD-workflow

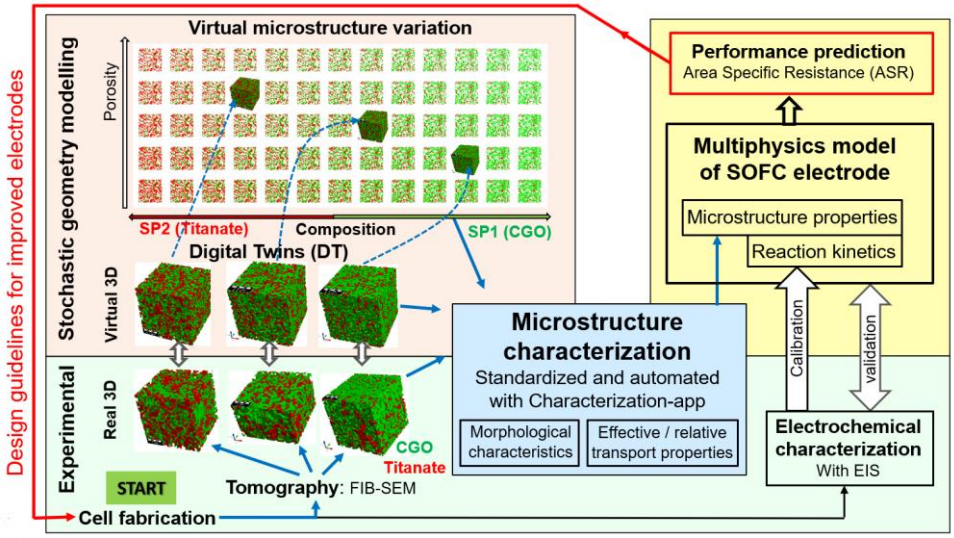

Fig. 2: Overview of the entire workflow for Digital Materials Design (DMD), which includes various methodological modules. The module for performance prediction with a multiscale-multiphysics electrode model, which is the main topic of the present paper, is highlighted in yellow. The methodological modules of the DMD workflow are described in great detail in separate papers, such as the module including materials processing and cell fabrication (see Burnat et al. [10,31]), the modules for imaging and standardized microstructure characterization (Marmet et al. [22] and Holzer et al. [32]), and the module of stochastic geometry modeling and associated realization of digital twins (Marmet et al. [20]).

The multiphysics electrode model presented in this contribution is a key-element of the Digital Materials Design (DMD) workflow illustrated in Fig. 2. This DMD-workflow was already described in previous publications [19], [20] and is briefly summarized in the following.

The basis for the DMD process is a set of fabricated solid oxide cells. The real microstructures are reconstructed using FIB-SEM tomography for a small number of fabricated cells representing a variation of the parameters to be optimized (e.g., composition and porosity). Stochastic digital microstructure twins with matching microstructure properties are then constructed for each real structure using a pluri-Gaussian method (PGM). Thereby, the PGM-script for virtual structure generation (developed in [20]) is available as a so-called GeoApp within the GeoDict software package (GeoDict release 2023 [33]). On that basis, the microstructure can be virtually varied for a large parameter space in a realistic way. The real and subsequently the virtual 3D structures need to be characterized quantitatively by means of image analysis and numerical simulations. A standardized and automated microstructure characterization tool has been developed within GeoDict [33] (see Marmet et al.

[22]), which enables the fast determination of an extensive set of microstructure properties relevant for SOC electrodes. The determined microstructure properties for the virtual structure variation can be used as an input for multiphysics electrode models as illustrated in Fig. 2. The multiphysics simulation model can be used to predict the impact of the microstructure variation on the electrode performance. This model-based performance prediction enables to establish the relationship between fabrication parameters, materials choices, microstructure properties and cell-performance. On this basis, design guidelines for the fabrication of electrodes with improved performance can be provided, which closes the loop of this iterative workflow. This paper is focused on the multiscale-multiphysics electrode model and especially on how the complex microstructure effects are incorporated to this continuum finite element (FE) model.

2.2.2. Stochastic microstructure modelling of LSCT-CGO electrodes and prediction of effective properties

In order to study the influence of the microstructure on the cell performance, the microstructures are systematically varied for porosity and LSCT-CGO composition using stochastic modelling. Moreover, the real and virtual structures are characterized to obtain the needed microstructure properties presented in section 1.2 as an input for the electrode model. Therefore, the corresponding parts of the DMD-workflow summarized in section 2.2.1 (and documented in more detail in Marmet et al. [20], [22], [19]) are applied to the LSCT-CGO electrodes studied in this contribution.

The real 3D microstructures are reconstructed by FIB-SEM tomography for a selection of the fabricated cells as described in section 2.1.2. 2D-orthoslices of the captured real 3D-sructures with different LSCT-CGO compositions are reported in the top row of Fig. 3. The imaging and microstructure characterization of these samples is described in more detail in section 10.3 in the PhD-thesis of Ph. Marmet [19]. With the methodologies presented in Marmet et al. [20], digital microstructure twins are constructed for each of the real microstructures with matching microstructure properties based on a pluri-Gaussian approach. A visual comparison of the 2D orthoslices of the digital twins is provided at the bottom row of Fig. 3. Note that the specific features are different, but the underlying statistics of the stochastic digital twins matches the real structures very well, resulting in very similar microstructure properties. A detailed description of the stochastic modelling of these microstructures can be found in section 10.3 of the PhD-thesis by Ph. Marmet [19] including a detailed comparison of the real and virtual structures.

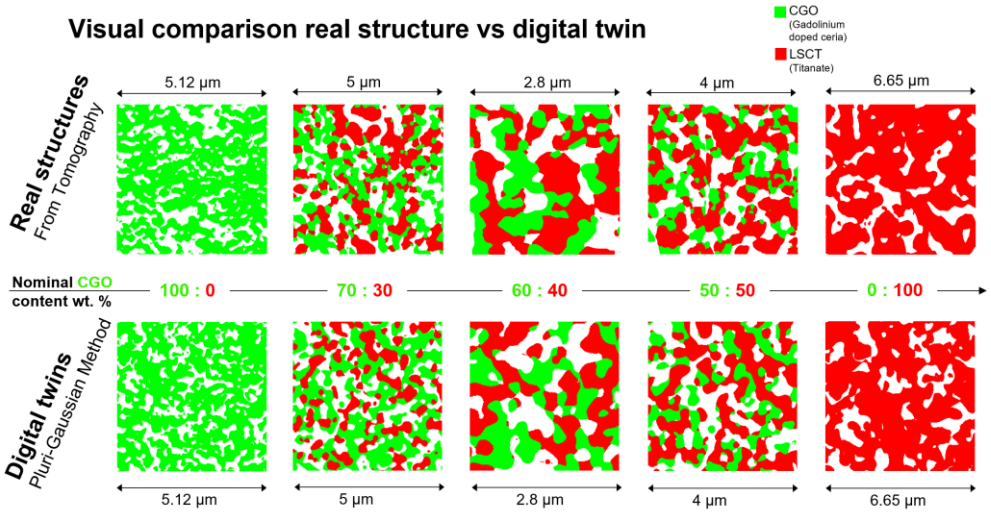

Fig. 3: Orthoslices for visual comparison of the real LSCT-CGO anode microstructures captured by tomography (top row) with the corresponding digital microstructure twins (bottom row) for different LSCT-CGO compositions.

Based on the set of digital microstructure twins visualized in the bottom row of Fig. 3, a virtual microstructure variation for different compositions and porosities was performed using the methods described in Marmet et al. [20]. Thereby, 98 3D-microstructures were generated. The corresponding 2D orthoslices are shown in Fig. 4. The orthoslices of the CGO100 and LSCT100 virtual microstructures are shown as well. The location of the real

microstructures of the used anchor points are indicated with black circles (note that the microstructure represented with the gray circle was excluded for the microstructure variation because of insufficient quality, see also section 10.3 in the PhD-thesis of Ph. Marmet [19] for further details). Note that the real structures CGO50-LSCT50 and CGO70-LSCT30 have almost the same porosity. Thus, effects related to the porosity variation are expected to be described less accurately compared to compositional changes with a much larger range of data. Nevertheless, the porosity variation can still be expected to provide the right optimization direction for a suitable porosity range.

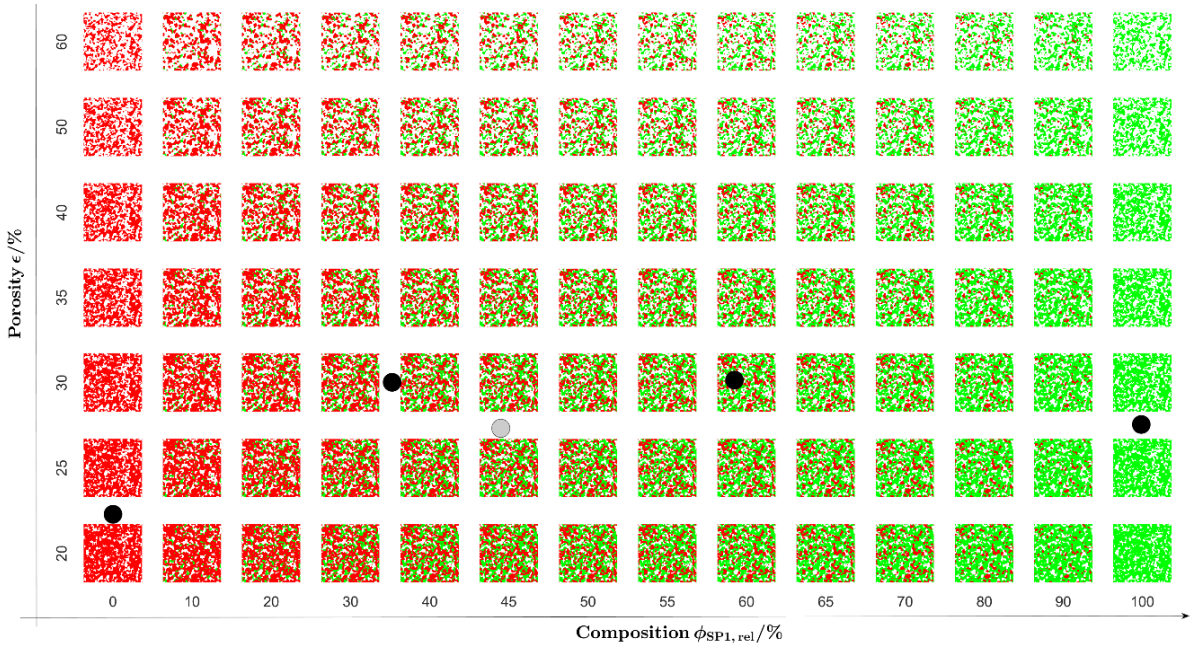

Fig. 4: 2D orthoslices captured in the center of the virtual 3D structures, representing variations of porosity and composition (i.e., relative solid phase volume fraction of CGO $\phi_{SP1,rel}$) based on the stochastic digital microstructure twins. The black dots correspond to the locations of the real structures (i.e. FIB tomography data) considered for the parameter variations: LSCT100 ($\phi_{SP1,rel} = 0\%$, $\varepsilon = 22.0\%$), CGO50-LSCT50 ($\phi_{SP1,rel} = 36.4\%$, $\varepsilon = 30.4\%$), CGO70-LSCT30 ($\phi_{SP1,rel} = 58.8\%$, $\varepsilon = 30.9\%$) and CGO100 ($\phi_{SP1,rel} = 100\%$, $\varepsilon = 27.7\%$). The grey dot is the excluded structure CGO60-LSCT40 ($\phi_{SP1,rel} = 44.4\%$, $\varepsilon = 27.1\%$).

The microstructure properties of the virtual microstructures reported in Fig. 4 are determined using the standardized microstructure characterization (characterization-app) introduced in Marmet et al. [22]). Thereby, GeoDict Cloud [33],[34] was used for a fast parallel characterization of the 98 microstructures. In the following the microstructure properties (introduced in section 1.2) needed for the parametrization of the multiphysics model are reported for the variation of the virtual microstructures as a function of the total volume fraction ϕ_{tot} and the relative volume fraction of CGO $\phi_{CGO,rel}$ (composition). In all the plots, the locations of the real structures are indicated with black circles.

The volume specific pore-CGO interface area $IA_{V,pore\text{-}CGO}$ is reported in Fig. 5 a) and correlates positively with the CGO-content and is maximal for a total solid volume fraction of about $\phi_{tot} = 50\%$. However, the surface of the data is relatively flat around the maximum and therefore leaves some flexibility for trade-offs. The volume specific pore-LSCT interface area $IA_{V,pore\text{-}LSCT}$ is reported in Fig. 5 b) and correlates positively with the LSCT-content.

International Journal of Multiphysics
Volume 18, No. 2s, 2024
ISSN: 1750-9548

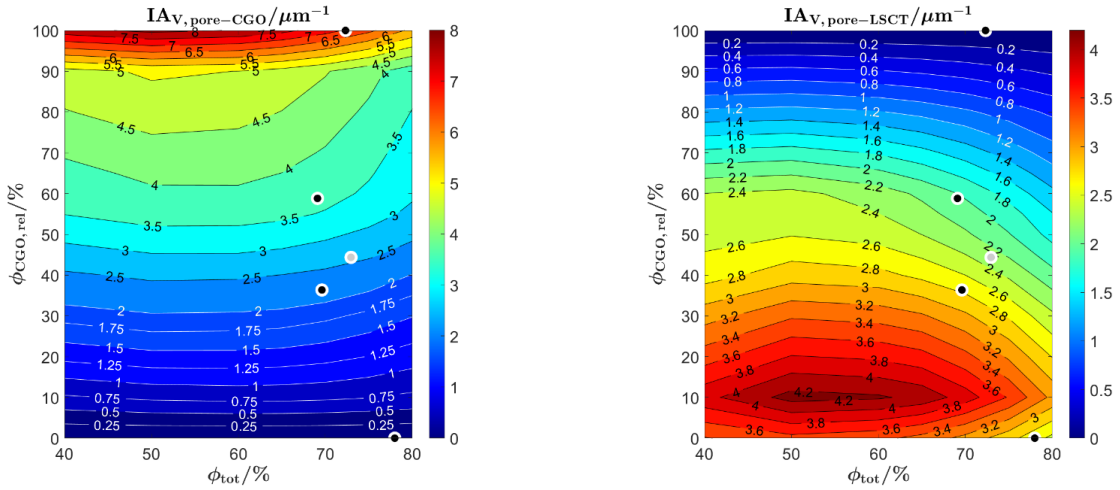

a) Volume specific interface area pore-CGO $IA_{\mathrm{V,pore\text{-}CGO}}$

b) Volume specific interface area pore-LSCT $IA_{\mathrm{V,pore\text{-}LSCT}}$

Fig. 5: Microstructure properties relevant for the reaction kinetics: Contour plots of the volume specific interface areas of a) pore-CGO and b) pore-LSCT as a function of the total solid volume fraction ϕ_{tot} (i.e., 100 – porosity) and the relative volume fraction of CGO $\phi_{\mathrm{CGO,rel}}$ (composition). The black dots represent the locations of the experimental data (FIB-tomography).

In Fig. 6 a), the relative ionic composite conductivities and in Fig. 6 b) the relative electronic composite conductivities are reported. The relative composite conductivities are defined in Eqs. 7 and 8 in section 3.2.1 (see also Marmet et al. [22]). The relative ionic composite conductivity is maximal for the highest total solid volume fraction (i.e., lowest porosity) and the highest CGO-content, because of the relatively high intrinsic ionic conductivity of CGO (see also section 1.2 and table 1). The relative electronic composite conductivity is maximal for the highest total solid volume fraction and the highest LSCT-content (i.e., lowest CGO-content), because of the relatively high intrinsic electronic conductivity of LSCT.

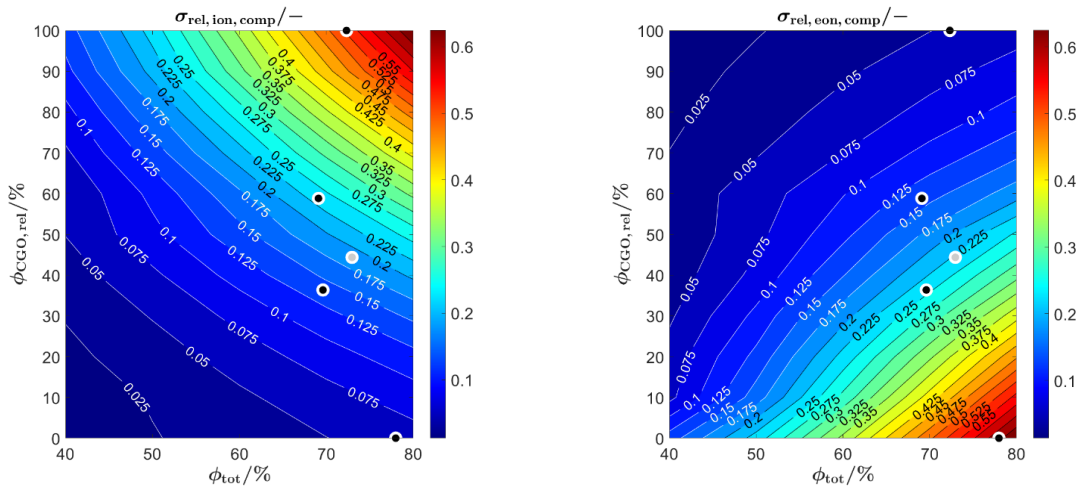

a) Relative ionic composite conductivity $\sigma_{\mathrm{rel,ion,comp}}$

b) Relative electronic composite conductivity $\sigma_{\mathrm{rel,eon,comp}}$

Fig. 6: Microstructure properties relevant for the charge transport: Contour plots of a) the relative ionic and b) the relative electronic (eon) composite conductivity as a function of the total solid volume fraction ϕ_{tot} (i.e., 100 – porosity) and the relative volume fraction of CGO $\phi_{\mathrm{CGO,rel}}$ (composition). The black dots represent the locations of the experimental data (FIB-tomography).

The contour plots of the microstructure properties relevant for the gas transport (according to the dusty-gas model [28], [22]) are plotted in Fig. 7. Note that the characteristic size of bulges and pores vary slightly as a function of the composition. Especially, the microstructure is coarser for compositions close to 100 % LSCT and finer for compositions close to 100 % CGO. However, the relative bulk diffusivity (Fig. 7 a)) and the relative Knudsen diffusivity (Fig. 7 b)) are non-dimensional and therewith almost independent from the composition. The Knudsen characteristic length (Fig. 7 c)) and the gas permeability (Fig. 7 d)) depend on the characteristic structure size and thus vary more significantly as a function of the composition, especially for compositions near 100 % CGO and 100 % LSCT.

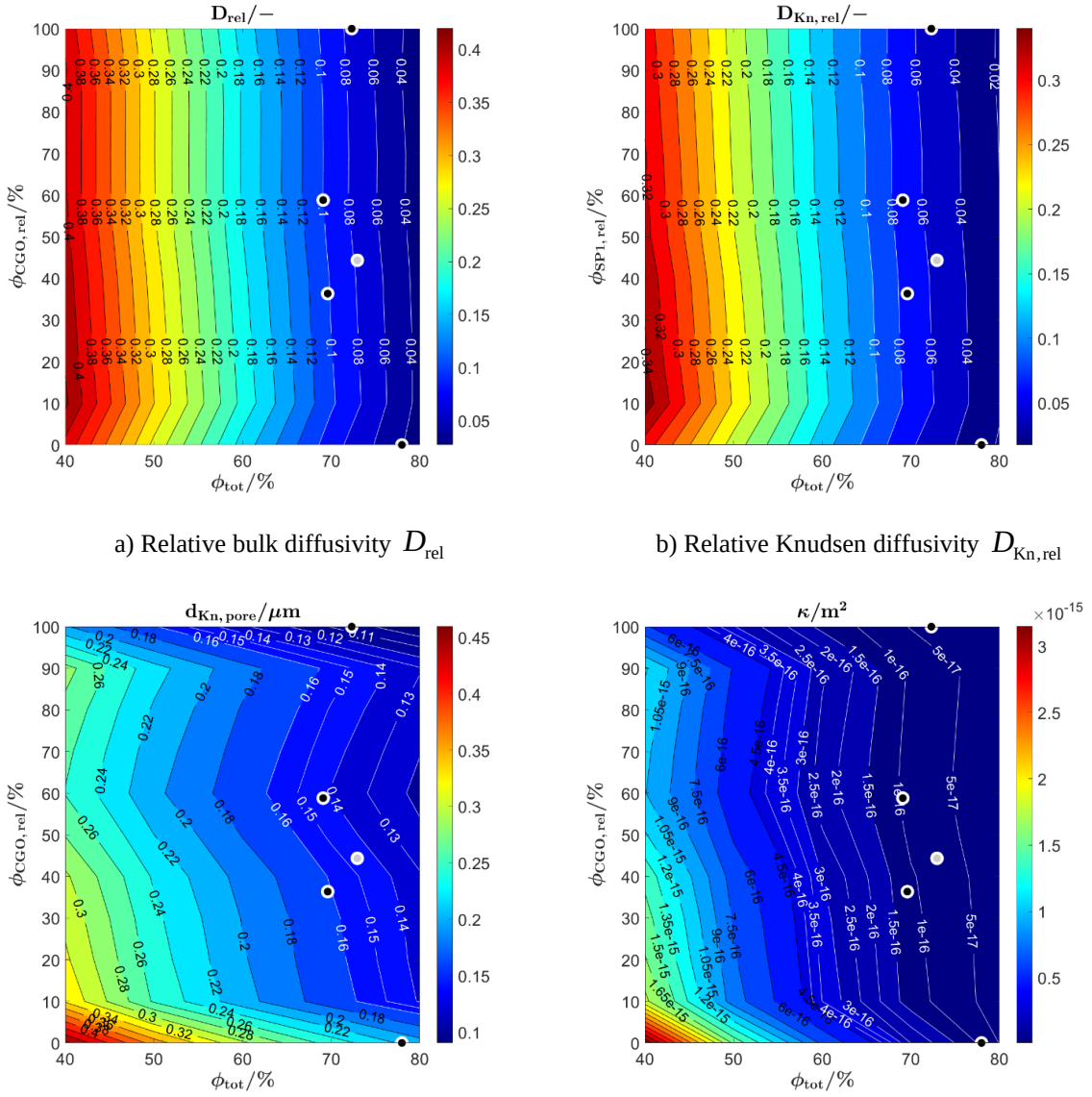

a) Relative bulk diffusivity D_{rel}

b) Relative Knudsen diffusivity $D_{\mathrm{Kn,rel}}$

c) Knudsen characteristic length $d_{\mathrm{pore,Kn}}$

d) Gas permeability κ

Figure 7: Microstructure properties relevant for the gas transport: Contour plots of the effective/relative transport properties of the pore-phase (for the parametrization of the dusty-gas model) as a function of the total solid volume fraction ϕ_{tot} (i.e. 100 – porosity) and the relative volume fraction of CGO $\phi_{\mathrm{CGO,rel}}$ (composition): a) relative bulk diffusivity, b) relative Knudsen diffusivity, c) Knudsen characteristic length (i.e., pore diameter) and d) gas permeability. The black dots represent the locations of the experimental data.

A more detailed description and discussion of the microstructure properties of the LSCT-CGO electrodes can be found in the sections 10.3.2 and 10.3.6 of the PhD-thesis by Ph. Marmet [19].

International Journal of Multiphysics
Volume 18, No. 2s, 2024
ISSN: 1750-9548

3. DEVELOPMENT OF A MULTISCALE-MUTLTIPHYSICS MIEC ELECTRODE MODEL

The contour plots of the microstructure properties as a function of the porosity and composition reported in section 2.2.2 already allow for a quantitative estimation of suitable parameters. However, the quantitative optimum of these trade-offs depends on the cell architecture (e.g., cell thickness, concept for current collection), the catalytic properties (e.g., use of an additional catalyst like Ni or noble metals) and operating conditions (e.g., temperature, fuel composition, fuel utilization). The most convenient way to solve such an optimization problem is to use multiphysics electrode models as e.g., suggested by Marmet et al. [28] for a pure CGO-electrode, for Ni-YSZ electrodes by Dierickx et al. [35] and Monaco et al. [36] and for a nickel-infiltrated CGO electrode by Kishimoto et al. [27].

In the current publication we develop a multiscale-multiphysics model for an LSCT-CGO electrode. Special emphasis is thereby laid on the appropriate incorporation of microstructure effects and their variation. Moreover, the reaction kinetics will be calibrated on measurements.

3.1. Model formulation

A multiphysics simulation model is used to predict the impact of the microstructure variation on the electrode performance (i.e., area specific resistance ASR_{tot}). Therefore, the 1D FE-model published in Marmet et al. [28] for porous ceria-based anodes (two-phase system) is adapted to describe the titanate-CGO-pore three-phase system. In contrast to CGO, where a good basis of experimental data is available for calibration of a complex model, such detailed information (e.g., for the reaction kinetics, vacancy concentrations and charge transport properties) is missing for titanate-CGO material systems. Therefore, the three-phase model is reformulated in a way which allows to calibrate the model consistently with the available experimental data.

A schematic representation of the involved physico-chemical processes used in this model is presented in Fig. 8. Thereby, the model is limited to the anode half-cell. The 1D FE model is implemented in the commercial software package COMSOL Multiphysics [37] in the steady state mode. The model consists of two computational domains (see Fig. 8). The domain $x = [0, L]$ is the porous LSCT-CGO anode functional layer (AFL), where the hydrogen oxidation reaction (HOR), the transport of the charge carriers in the LSCT-CGO composite and the transport of the gas species in the porous media take place. As the pores and the LSCT- and CGO-phase are not spatially resolved, the effects of the porous microstructure are considered by using the effective microstructure properties determined in section 2.2.2. The domain $x = [-L_{\text{Stag}}, 0]$ represents the stagnant gas layer at the interface between the gas flow channel and the anode functional layer. There, gas species diffusion corresponding to a button cell setup with an excess flowrate is considered (see also Marmet et al. [28]). The electrolyte and the current collector layer (CCL) are modelled as boundary conditions.

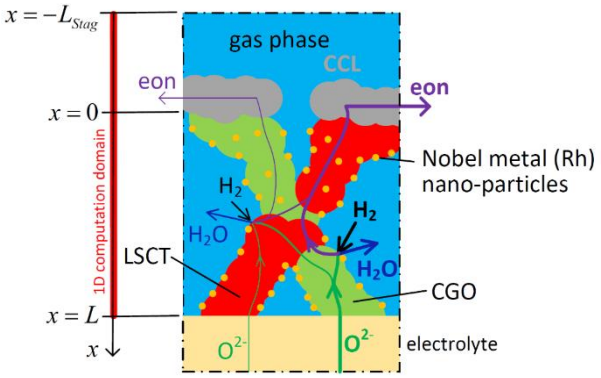

Fig. 8: Illustration of the three-phase simulation model for a simplified microstructure scenario, showing reaction locations and transport pathways for an anode with two solid MIEC-phases and a pore-phase. Legend: CGO (green), LSCT/titanite (red), pore and gas channel (blue), current collector layer (CCL, gray) and catalyst nanoparticles (orange dots). Arrows mark the transport pathways of ions (green), electrons (eon / purple) and gas species (black).

There are three different reaction sites considered for the hydrogen oxidation reaction (HOR), namely at the pore-CGO interface, the pore-LSCT-interface and at the three-phase boundaries (TPB). The reaction kinetics are thereby enhanced by a fine dispersed noble metal catalyst (i.e., Rh for the current study) and the corresponding reaction kinetics are calibrated to dedicated experiments (see section 3.3.2).

The charge transport is modelled by Ohms law, using an ionic and electronic potential. This approach of modelling the charge transport represents a considerable simplification of the transport mechanism in MIECs, which are governed by drift and diffusion (as e.g., modelled for pure CGO-electrodes in Marmet et al. [28]). However, it is currently not clear how the drift and diffusion transport evolve across the CGO-LSCT boundaries, and a considerable amount of basic research is still needed for the LSCT-CGO material system (and also for perovskite-CGO composites in general). Therefore, we stick to this simplified but consistent description of charge transport by Ohms law. The microstructure effects including the LSCT:CGO composition is captured using the relative ionic and electronic composite conductivities as introduced in Marmet et al. [22] (see also Eqs. 7,8 and corresponding discussion).

The gas transport is described with the dusty-gas model in the same way as for the CGO-electrode model reported in Marmet et al. [22].

3.2 Equations for the three-phase electrode model

3.2.1 Basic equations for transport and charge transfer

The steady state continuity equations for electrons and ions reads:

$$\nabla \cdot J_{\text{ion}} = i_{\text{ion}} \quad (1)$$

$$\nabla \cdot J_{\text{eon}} = i_{\text{eon}} . \quad (2)$$

The source terms for the ionic current i_{ion} and the electronic current i_{eon} are given by:

$$i_{\text{ion}} = -i_{\text{HOR}} \quad (3)$$

$$i_{\text{eon}} = i_{\text{HOR}} , \quad (4)$$

where i_{HOR} is the total reaction rate, which can consist of different reaction pathways (e.g., surface reactions and TPB) as specified in Eq. 9. The total reaction rate i_{HOR} is expressed as a source term because of the used 1D setup. Note that the total reaction rate i_{HOR} and the resulting ionic i_{ion} and electronic i_{eon} source terms are formulated as an electric current source with units A/m^3 and not in terms of the species concentrations for electrons and oxygen ions and therewith, there is no factor two for the ionic species in Eq. 3.

The ionic and electronic current densities read:

$$J_{\text{ion}} = -\sigma_{\text{eff,ion,comp}} \nabla \phi_{\text{ion}} \quad (5)$$

$$J_{\text{eon}} = -\sigma_{\text{eff,eon,comp}} \nabla \phi_{\text{eon}} , \quad (6)$$

where ϕ_{ion} is the ionic and ϕ_{eon} the electronic potential. $\sigma_{\text{eff,ion,comp}}$ and $\sigma_{\text{eff,eon,comp}}$ are the ionic and electronic composite conductivities for the combined titanate-CGO solid-phase and are given by (see also Marmet et al. [22]):

$$\sigma_{\text{eff,ion,comp}} = \sigma_{\text{rel,ion,comp}} \sigma_{0,\text{ion,CGO}} \quad (7)$$

$$\sigma_{\text{eff,eon,comp}} = \sigma_{\text{rel,eon,comp}} \sigma_{0,\text{eon,LSCT}} , \quad (8)$$

where $\sigma_{\text{rel,ion,comp}}$ is the relative ionic composite conductivity, $\sigma_{\text{rel,eon,comp}}$ the relative electronic composite conductivity, $\sigma_{0,\text{ion,CGO}}$ the intrinsic ionic conductivity of CGO and $\sigma_{0,\text{eon,LSCT}}$ the intrinsic electronic conductivity of LSCT. Note that the relative ionic composite conductivity $\sigma_{\text{rel,ion,comp}} = f(\lambda_{\text{ion}})$ is a function of the ratio of the intrinsic ionic conductivities $\lambda_{\text{ion}} = \frac{\sigma_{0,\text{ion,LSCT}}}{\sigma_{0,\text{ion,CGO}}}$ and the relative electronic composite conductivity $\sigma_{\text{rel,eon,comp}} = f(\lambda_{\text{eon}})$ is a function of the ratio of the intrinsic electronic conductivities $\lambda_{\text{eon}} = \frac{\sigma_{0,\text{eon,CGO}}}{\sigma_{0,\text{eon,LSCT}}}$.

The definitions for the relative and effective composite conductivities were introduced in Marmet et al. [22] in a more general way.

The total reaction rate i_{HOR} (Eq. 9) consists of different possible reaction pathways at the surfaces of CGO (Eq. 10) and LSCT (Eq. 11) and at the TPBs (Eq. 12). All contributions are formulated with Butler-Volmer kinetics:

$$i_{\text{HOR}} = i_{\text{SR,CGO}} + i_{\text{SR,LSCT}} + i_{\text{TPB}} \quad (9)$$

$$i_{\text{SR,CGO}} = i_{0,\text{SR,CGO}} \left(\exp\left(\alpha_{\text{CGO}} \frac{n_{\text{eon}} F \eta_{\text{act}}}{R_{\text{gas}} T} \right) - \exp\left(-(1-\alpha_{\text{CGO}}) \frac{n_{\text{eon}} F \eta_{\text{act}}}{R_{\text{gas}} T} \right) \right) \quad (10)$$

$$i_{\text{SR,LSCT}} = i_{0,\text{SR,LSCT}} \left(\exp\left(\alpha_{\text{LSCT}} \frac{n_{\text{eon}} F \eta_{\text{act}}}{R_{\text{gas}} T} \right) - \exp\left(-(1-\alpha_{\text{LSCT}}) \frac{n_{\text{eon}} F \eta_{\text{act}}}{R_{\text{gas}} T} \right) \right) \quad (11)$$

$$i_{\text{TPB}} = i_{0,\text{TPB}} \left(\exp\left(\alpha_{\text{TPB}} \frac{n_{\text{eon}} F \eta_{\text{act}}}{R_{\text{gas}} T} \right) - \exp\left(-(1-\alpha_{\text{TPB}}) \frac{n_{\text{eon}} F \eta_{\text{act}}}{R_{\text{gas}} T} \right) \right), \quad (12)$$

where T is the temperature, R the ideal gas constant, F the Faraday constant, n_{eon} the number of participating electrons in the reaction and α_{CGO}, α_{LSCT}, and α_{TPB} are the charge transfer coefficients and η_{act} is the activation overpotential defined in Eq. 13. The exchange current densities $i_{0,\text{SR,CGO}}$, $i_{0,\text{SR,LSCT}}$ and $i_{0,\text{TPB}}$ for the three reaction pathways reported in Eqs. 10-12 are formulated to fit the observations of the experimental characterization. This calibration is reported in section 3.3.2.

The activation overpotential is defined as:

$$\eta_{\text{act}} = \phi_{\text{eon}} - \phi_{\text{ion}}. \quad (13)$$

With this formulation, we assume that there is no direct link of the gas diffusion impedance to the extension of the reaction zone. Within the porous MIEC anode, the transport and the reaction of the gas species need to be described. The continuity equations for the gas species reads:

$$\nabla \cdot N_1 = R_1 \quad (14)$$

$$\nabla \cdot N_2 = R_2 \quad (15)$$

where N_1, N_2 are the molar flux densities and R_1, R_2 are the reaction rates for hydrogen (species 1) and water vapor (species 2) , respectively. Thereby, the consumption rate of hydrogen is equal to the production rate of water vapor, which is related to the current source term in the following way:

$$R_2 = -R_1 = \frac{i_{\mathrm{HOR}}}{2F}, \qquad (16)$$

where i_{HOR} is defined in Eq. 9. The molar flux densities N_1 and N_2 are modelled according to the Dusty-gas model (DGM) as documented in a previous publication by Marmet et al. [28]. For this contribution, we restrict the discussion on how the microstructure properties enter the DGM, which accounts for bulk and Knudsen diffusion. The bulk-diffusion contribution is governed by the effective binary diffusion coefficient $D_{12,\mathrm{eff}}$:

$$D_{12,\mathrm{eff}} = D_{\mathrm{rel}} D_{12,0}, \qquad (17)$$

where $D_{12,0}$ is the intrinsic binary diffusion coefficient between hydrogen and water determined according to Fuller et al. [38] and the relative diffusivity D_{rel} for the pore-phase accounts for the effect of the microstructure.

The effect of the Knudsen diffusion is governed by the effective Knudsen diffusion coefficients for hydrogen $D_{1,\mathrm{Kn,eff}}$ and water $D_{2,\mathrm{Kn,eff}}$, respectively:

$$D_{i\mathrm{Kn,eff}} = D_{\mathrm{Kn,rel}} D_{i\mathrm{Kn},0}, \qquad (18)$$

where $D_{i,\mathrm{Kn},0}$ is the intrinsic Knudsen diffusion coefficient according to the kinetic theory of gases [39], $D_{\mathrm{Kn},rel}$ is the microstructure factor for the Knudsen diffusion mechanism and i denotes species 1 (hydrogen) or 2 (water vapor). It is worth noting that the intrinsic (and thus also the effective) Knudsen diffusion coefficient is proportional to a characteristic pore diameter $d_{\mathrm{Kn,pore}}$ of the porous structure, while the effective binary diffusion coefficient $D_{12,\mathrm{eff}}$ is size independent and does only depend on the morphology of the microstructure.

Finally, the DGM includes a convective part, which is governed by the gas-flow permeability κ of the microstructure and the dynamic viscosity of the gas mixture μ_{visc}. A detailed description how these microstructure properties are determined can be found in Marmet et al. [22].

3.2.2 Boundary conditions

The boundary conditions for the charge transport equations are formulated in the following. At the AFL/CCL interface at x = 0, the ions are blocked:

$$. J_{\mathrm{ion}}(x=0) = 0. \qquad (19)$$

At the AFL/electrolyte interface at x = L, the electrons are blocked:

$$J_{\mathrm{eon}}(x=L) = 0. \qquad (20)$$

Per definition, we set the electronic potential at the interface to the CCL to ground:

$$\phi_{\mathrm{eon}}(x=0) = 0. \qquad (21)$$

The ionic potential at the AFL/electrolyte interface is set to a parameter $\eta_{\mathrm{HOR+chrg\,tpt}}$ combining the overpotential due to charge transport and reaction resistance and is adapted to result in a prescribed current density J_{charge} using a global constraint within Comsol Multiphysics:

$$\phi_{\text{ion}}\left(x=L\right)=\eta_{\text{HOR+chrg tpt}}. \qquad (22)$$

Furthermore, the boundary conditions for the gas transport are reported in the following. The goal of the simplified model for the gas concentration overpotential as described in Marmet et al. [22] is to mimic an ideal fuel supply, but respecting the diffusion limitations in the stagnant gas layer. Therefore, the concentrations at the end of the stagnant gas layer at $x=-L_{\text{Stag}}$ are fixed to the given gas concentrations of the fuel supply of hydrogen $c_{1,0}$ and water vapour $c_{2,0}$:

$$c_1\left(x=-L_{\text{Stag}}\right)=c_{1,0} \qquad (23)$$

$$c_2\left(x=-L_{\text{Stag}}\right)=c_{2,0}. \qquad (24)$$

A zero-flux boundary condition is implemented for all gas species at the AFL / electrolyte interface, as the non-porous electrolyte is assumed to be impermeable for the gas species:

$$N_1\left(x=L\right)=0 \qquad (25)$$

$$N_2\left(x=L\right)=0. \qquad (26)$$

3.2.3 Overpotentials and contributions to the area specific resistance (ASR)

The local gas overpotential in the porous electrode is given by:

$$\eta_{\text{gas}}=\frac{R_{\text{gas}}T}{2F}\ln\left(\frac{x_1(0)\cdot x_2(x)}{x_1(x)\cdot x_2(0)}\right), \qquad (27)$$

where $x_1(0)$ and $x_2(0)$ are the hydrogen and water fractions at the electrode surface. The averaged gas overpotential of the porous electrode can be determined as follows:

$$\eta_{\text{gas,porous,avg}}=\frac{1}{J_{\text{charge}}}\int_0^L\frac{\partial\eta_{\text{gas}}}{\partial x}J_{\text{c1}}2F dx, \qquad (28)$$

where J_{c1} is the hydrogen species flux.

The gas overpotential in the stagnant gas layer is given by:

$$\eta_{\text{gas,stag}}=\frac{R_{\text{gas}}T}{2F}\ln\left(\frac{x_{1,0}\,x_2(0)}{x_1(0)x_{2,0}}\right), \qquad (29)$$

where $x_{1,0}$ is the hydrogen fraction and $x_{2,0}$ is the water fraction of the supplied fuel and $x_1(0)$ and $x_2(0)$ are the hydrogen and water fractions at the electrode surface. This formulation enables to distinguish between the gas concentration overpotential of the porous electrode and the stagnant gas layer. The total averaged gas concentration overpotential reads:

$$\eta_{\text{gas,avg}}=\eta_{\text{gas,stag}}+\eta_{\text{gas,porous,avg}}. \qquad (30)$$

The gas concentration contribution to the ASR is given by:

$$ASR_{\text{gas}}=\frac{\partial\eta_{\text{gas,avg}}}{\partial J_{\text{charge}}}. \qquad (31)$$

The combined effect of charge transport and reaction resistance is given by:

$$ASR_{\mathrm{HOR+chrg\,tpt}} = \frac{\partial \eta_{\mathrm{HOR+chrg\,tpt}}}{\partial J_{\mathrm{charge}}}, \qquad (32)$$

where $\eta_{\mathrm{HOR+chrg\,tpt}}$ results from the constraint used for the boundary condition in Eq. 22 for a fixed current density. The total area specific resistance results in:

$$ASR_{\mathrm{tot}} = ASR_{\mathrm{HOR+chrg\,tpt}} + ASR_{\mathrm{gas}}. \qquad (33)$$

The overpotentials for the reaction and the charge transport can be formulated separately. The overpotential of for the charge transport reads.

$$\eta_{\mathrm{chrg\,tpt,avg}} = \frac{1}{J_{\mathrm{charge}}}\left(\int_0^L E_{\mathrm{ion}} J_{\mathrm{ion}}\, dx + \int_0^L E_{\mathrm{eon}} J_{\mathrm{eon}}\, dx\right). \qquad (34)$$

The corresponding ASR contribution is given by:

$$ASR_{\mathrm{chrg\,tpt}} = \frac{\partial \eta_{\mathrm{chrg\,tpt,avg}}}{\partial J_{\mathrm{charge}}}. \qquad (35)$$

The average reaction overpotential $\eta_{\mathrm{HOR,avg}}$ is calculated from the local reaction overpotential η_{act}:

$$\eta_{\mathrm{act,avg}} = \frac{1}{J_{\mathrm{charge}}}\int_0^L \eta_{\mathrm{act}} i_{\mathrm{HOR}}\, dx. \qquad (36)$$

The corresponding ASR contribution is given by:

$$ASR_{\mathrm{HOR}} = \frac{\partial \eta_{\mathrm{HOR,avg}}}{\partial J_{\mathrm{charge}}}. \qquad (37)$$

Note the derivations for the determination of the ASR are approximated numerically in the following way:

$$ASR_i = \frac{\eta_{\mathrm{i}}(J_{\mathrm{charge}} + \Delta J_{\mathrm{charge}}) - \eta_{\mathrm{i}}(J_{\mathrm{charge}})}{\Delta J_{\mathrm{charge}}}, \qquad (38)$$

where a value of $\Delta J_{\mathrm{charge}} = 10\,\mathrm{A/m^2}$ was used.

3.3. Parametrization of the model

3.3.1 Summary of the used model parameters

In order to obtain quantitively meaningful simulation results, the electrode model needs to be parametrized appropriately. Thereby, three types of parameters are needed:

- The effect of the microstructure enters the model using the effective microstructure properties described in section 2.2.2 for gas and charge transport and the density of available reaction sites for the reaction kinetics.
- Intrinsic material properties for the transport of charge carriers (i.e., intrinsic ionic and electronic conductivities) and for the gas transport (i.e., intrinsic diffusivities and viscosity). These parameters are reported in table 1. The intrinsic Knudsen diffusion coefficients depends on the pore diameter (i.e., is not constant) and is determined as reported in Marmet et al. [28].
- The reaction kinetics for the Rh-impregnated LSCT-CGO anodes is determined based on experimental performance characterization by electrochemical impedance spectroscopy. The corresponding kinetic parameter are reported in table 1 and the calibration process is described in section 3.3.2.
- The operating conditions, i.e., the operating temperature, the current density and the fuel composition (humidity of hydrogen) need to be specified. The temperature is reported in table 1, while the other operating conditions are varied and thus reported in the results and discussion section 4.

Table 1: Parameters used for the multiphysics anode model. The parameters calibrated with the EIS-measurements are indicated with (*) in the reference-column. The intrinsic Knudsen diffusion coefficients depend on the pore diameter and are determined as reported in Marmet et al. [28].

Parameter	Value	Description	Reference
k_0	200e6	Kinetic fit-parameter	(*)
$k_{\mathrm{SR,CGO}}$	$4\cdot\exp\left(\frac{j_{\mathrm{current}}}{8000\,\mathrm{A/m^2}}\right)$	Kinetic fit-parameter surface reaction of CGO	(*)
$k_{\mathrm{SR,LSCT}}$	$0.18\cdot\exp\left(\frac{j_{\mathrm{current}}}{8000\,\mathrm{A/m^2}}\right)$	Kinetic fit-parameter surface reaction of LSCT	(*)
$k_{\mathrm{SR,LSCT/CGO}}$	3.4	Kinetic fit-parameter surface reaction of LSCT, influence of CGO	(*)
k_{TPB}	0	Kinetic fit-parameter for the TPB-reaction	(*)
m_{H2O}	0.3620	Power-law water fraction dependency	(*)
α_{CGO}	0.5	BV parametrization CGO surface reaction	(*)
α_{LSCT}	0.5	BV parametrization LSCT surface reaction	(*)
n_{eon}	2	Number of involved electrons	-
$IA_{\mathrm{V,pore\text{-}CGO,ref}}$	$2.1\,\mu\mathrm{m}^{-1}$	Reference volume specific pore-CGO interface area	definition
$IA_{\mathrm{V,pore\text{-}CGO,ref}}$	$2.1\,\mu\mathrm{m}^{-1}$	Reference volume specific pore-LSCT interface area	definition
T	850 °C	Temperature	-
$\sigma_{\mathrm{0,eon,LSCT}}$	$18.3\,\mathrm{S/cm}$	Intrinsic electronic conductivity of LSCT	[10,40]
$\sigma_{\mathrm{0,eon,CGO}}$	$1.83\,\mathrm{S/cm}$	Intrinsic electronic conductivity of CGO	[41]
$\sigma_{\mathrm{0,ion,LSCT}}$	$0.013\,\mathrm{S/cm}$	Intrinsic ionic conductivity of LSCT	[10,40]

$\sigma_{0,ion,CGO}$	$0.13\,S/cm$	Intrinsic ionic conductivity of CGO	[41]
$D_{12,0}$	$9.3363\cdot10^{-4}\,m^2/s$	Binary intrinsic diffusivity H_2 / H_2O	[28,38]
μ_{visc}	$2.2\cdot10^{-5}\,Pa\cdot s$	Dynamic viscosity of hydrogen	[42]
L_{Stag}	$0.5\,mm$	Stagnant gas layer thickness	estimation

3.3.2 Calibration of the reaction kinetics

In Fig. 9, a typical EIS-spectrum is shown for LSCT-CGO anodes with noble metal catalyst Rh-impregnation by reporting the Nyquist-plot and the imaginary part plot. Thereby, three major features are detected which are named as low frequency arc (LF-arc), middle frequency arc (MF-arc) and high frequency arc (HF-arc) according to their frequency range. The physical meaning of the different arcs have been thoroughly studied in the PhD-thesis of Ph. Marmet [19] based on a large number of EIS-measurements for different cells and operating conditions. The most important results are summarized in the following:

- The LF-arc is associated with the anode and is composed of a pore-CGO interface reaction / chemical capacitance process and a gas impedance process.
- The MF-arc is related to an anode and a cathode process. The anode part of the MF-arc is probably related to a HOR process at the pore-LSCT interface or/and the TPBs and to the ionic charge transport resistance within LSCT.
- The HF-arc is associated with an interface effect, most probably an interface resistance at the AFL/electrolyte interface.

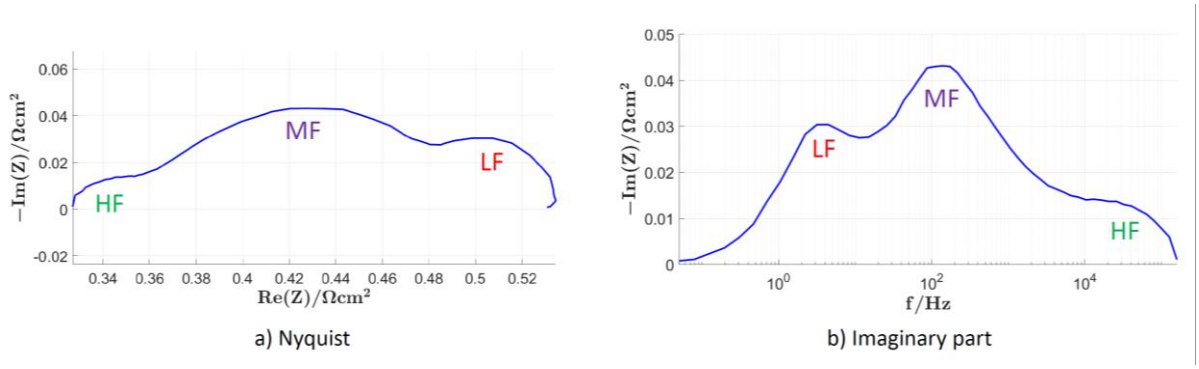

Fig. 9: Example of a typical EIS-spectrum of an LSCT-CGO anode with a composition of CGO:LSCT = 30:70 wt.% (Nr. BC5-2021-034) for $T=850^{\circ}C$, $OCV_{ref}=1100mV$ (i.e., water content 2.7 %) and I = 300 mA. a) Nyquist-plot, b) imaginary part plot. Legend: LF = low frequency, MF = middle frequency and HF = high frequency arc.

The following assumptions and procedure have been used for the model calibration:

- The reaction kinetics of the HOR is the process with the highest uncertainty. Therefore, the kinetic parameters and their dependency on the operating conditions are fitted. The intrinsic properties for the charge and gas transport are estimated from the literature as reported in table 1.
- To calibrate the reaction kinetics of the anode, the resulting total anode ASR from the simulation is fitted to the measured polarization resistance corrected by an estimated cathode polarization part. The relatively small HF-contribution is not removed and lumped to the anode polarization resistance. Moreover, the relative contributions of the CGO- and LSCT-surface reactions are estimated from the measurements and fitted as well.
- For the calibration, EIS-measurements for four button cells with nominal compositions CGO:LSCT = $[0:100,20:80,30:70,50:50,60:40]wt.\%$ were used, which corresponds approximately to the

volumetric composition of CGO:LSCT = $[0:100,15:85,23:77,41:59,51:49]\text{vol.\%}$. The cells are measured at different current densities $J=[0,0.208,0.625]\text{A/cm}^2$ and different reference OCVs $OCV_{\text{ref}}=[1050,1100]\text{mV}$ corresponding to water fractions of $x_2=[0.07,0.027]$.

The exchange current densities for the three reaction pathways reported in Eqs. 10-12 (section 3.2.1) are formulated to fit the observations of the experimental characterization as reported in the following:

$$i_{0,\text{SR,CGO}}=k_0\,x_2^{m_{\text{H2O}}}k_{\text{SR,CGO}}\frac{IA_{\text{V,pore-CGO}}}{IA_{\text{V,pore-CGO,ref}}} \tag{39}$$

$$i_{0,\text{SR,LSCT}}=k_0\,x_2^{m_{\text{H2O}}}k_{\text{SR,LSCT}}\frac{IA_{\text{V,pore-LSCT}}}{IA_{\text{V,pore-LSCT,ref}}}\left(1+k_{\text{SR,LSCT/CGO}}\frac{IA_{\text{V,pore-CGO}}}{IA_{\text{V,pore-CGO,ref}}}\right) \tag{40}$$

$$i_{0,\text{TPB}}=0. \tag{41}$$

The exchange current density for the TPB reaction (Eq. 12) is set to zero assuming that there is no distinct reaction pathway related to the TPBs. The expressions for the surface reactions contain the same rate constant k_0 and the same dependency on the water fraction x_2 using a power law with the exponent m_{H2O}. The exchange current densities for the CGO surface reaction $i_{0,\text{SR,CGO}}$ (Eq. 11) is assumed to be proportional to the volume specific pore-CGO interface area $IA_{\text{V,pore-CGO}}$. The exchange current densities for the LSCT surface reaction $i_{0,\text{SR,LSCT}}$ is assumed to be proportional to the volume specific pore-LSCT interface area $IA_{\text{V,pore-LSCT}}$ and additionally catalyzed by the adjacent CGO-phase and thus, also depending on the volume specific pore-CGO interface area $IA_{\text{V,pore-CGO}}$. All interface properties are normed to a typical reference value. Therewith the used rate constants $k_{\text{SR,CGO}}$, $k_{\text{SR,LSCT}}$ and $k_{\text{SR,LSCT/CGO}}$ are comparable and provide an estimate on the importance of the corresponding reaction pathways.

4. RESULTS AND DISCUSSION

The multiscale multiphysics model allows for a quantitative assessment of the different physico-chemical phenomena involved. Especially, the different components of area specific resistances (ASR) due to limitations of (gas and charge) transport in the bulk and electrochemical reactions at pore-solid interfaces and their dependency on the microstructure, cell design and operating conditions is presented. First, the different contributions to the total anode ASR are reported as a function of porosity and composition for a fixed anode layer thickness of $L=15\,\mu\text{m}$ in section 4.1. In section 4.2, the optimal anode layer thickness and associated performance is reported as a function of porosity and composition for the full virtual LSCT-CGO microstructure variation. Moreover, the influence of the operating conditions (section 4.3) and the characteristic structure size (section 4.4) is presented.

4.1 Simulation results for a fixed anode layer thickness of $L=15\,\mu\text{m}$.

In Fig. 10, the different contributions to the total anode ASR are reported for the virtual LSCT-CGO microstructure variation for the total solid volume fraction ϕ_{tot} (or porosity ε, respectively) and the LSCT-CGO composition $\phi_{\text{CGO,rel}}$ reported in section 2.2.2 for a fixed anode layer thickness of $L=15\,\mu\text{m}$. The HOR-ASR (Fig. 10 a)) negatively correlates with the CGO-content because CGO owns the higher electrochemical activity compared to LSCT. The minimal values are observed for the total volume fraction of about $\phi_{\text{tot}}=60\%$, which is slightly higher than the maximum of the volume specific pore-CGO and pore-LSCT interface areas reported in

Fig. 5 a) and b). The data surface for the interface areas is very flat around the maximum at $\phi_{tot} = 50\%$. Thus, the larger extension of the reaction zone associated with higher composite conductivities for higher ϕ_{tot} results in this shift.

The ASR due to charge transport (Fig. 10 b)) negatively correlates with the CGO-content and ϕ_{tot} and corresponds inversely to the relative ionic composite conductivity $\sigma_{rel,ion,comp}$ reported in Fig. 6 a).

The ASR due to the gas transport (gas concentration impedance, (Fig. 10 c)) decreases sharply towards low porosities (i.e., large ϕ_{tot}). This is a consequence of the low relative diffusivity and the smaller characteristic pore-size (resulting in a lower Knudsen diffusivity) associated with low porosities as reported in Fig. 7. The strong increase of the gas impedance towards high CGO-contents is because of the finer microstructure observed for high CGO-contents, which results in smaller characteristic pore-sizes and thus higher transport resistances due to Knudsen diffusion.

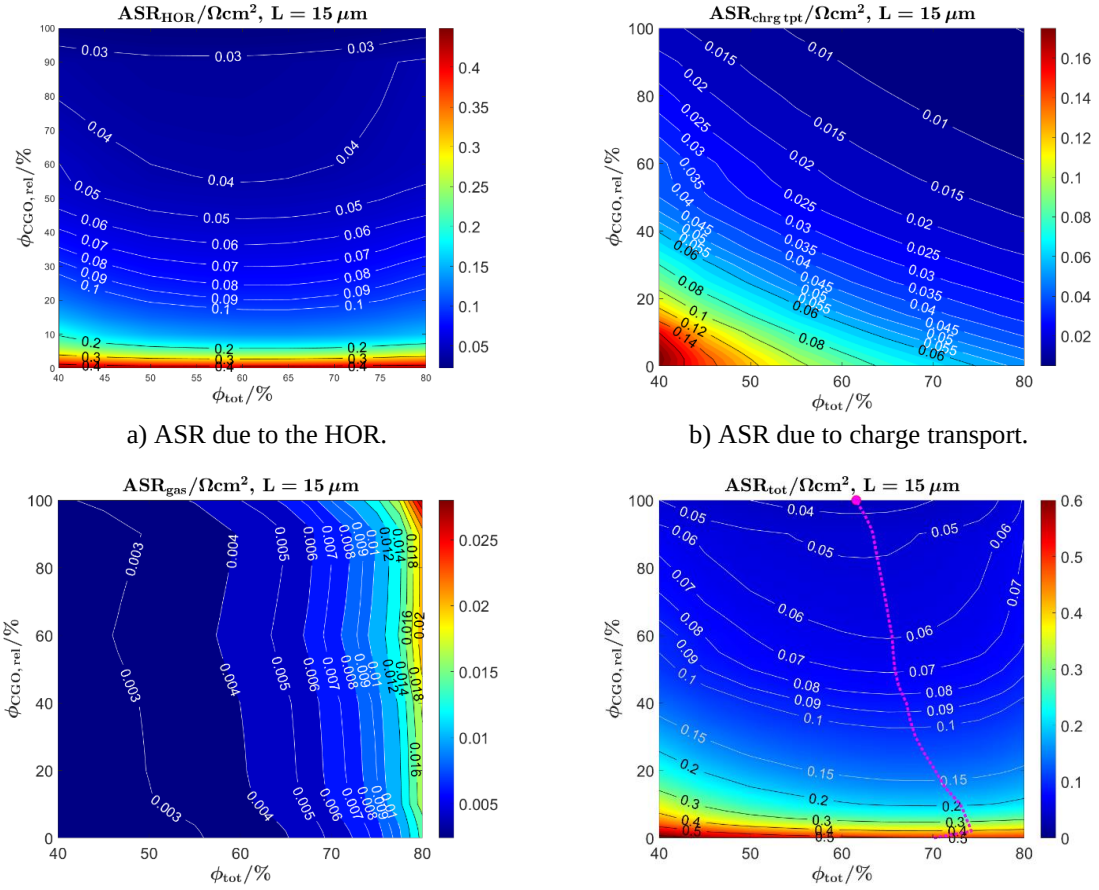

a) ASR due to the HOR.

b) ASR due to charge transport.

c) ASR due to gas transport.

d) Total anode ASR.

Fig. 10 Simulation results for a fixed AFL-thickness $L = 15\,\mu m$ as a function of total solid volume fraction ϕ_{tot} (i.e., 100 – porosity) and composition $\phi_{CGO,rel}$. Different resistive components contributing to the total ASR of the anode are computed under fixed conditions with $OCV_{ref} = 1050\,mV$ (water content 7 %) and $J = 0.208\,A/cm^2$. Contour plots of a) the ASR due to the HOR, b) the ASR due to the charge transport, c) the ASR due to gas transport, and d) the total anode ASR, where the dashed magenta line represents the minimal ASR and optimal ϕ_{tot} upon a compositional variation. The iso-lines plotted in white have a smaller spacing in order to provide additional information for the regions with lower values.

The resulting total anode ASR (Fig. 10 d)) negatively correlates with the CGO-content, following the contributions of the HOR (Fig. 10 a)) and the charge transport resistance (Fig. 10 b)). A sharp increase is observed for CGO-contents below 20 vol.%. In contrast, the data-surface is very flat for a CGO-content above 60 vol.%, which opens the possibility for trade-offs with additional goals like a good degradation behavior or improved current collection functionality of the AFL, both associated with the LSCT-phase. The dashed magenta line represents the minimal ASR and optimal total solid volume fraction ϕ_{tot} upon a compositional variation. For high CGO-contents, a relatively high porosity around 35 % (i.e., $\phi_{\text{tot}} = 65\%$) is favorable in order to have a large surface area and a good gas transport. For low CGO-contents, a porosity below 30 % is favorable to maintain a sufficient ionic conductivity.

4.2 Variation of total ASR for the optimal layer thickness

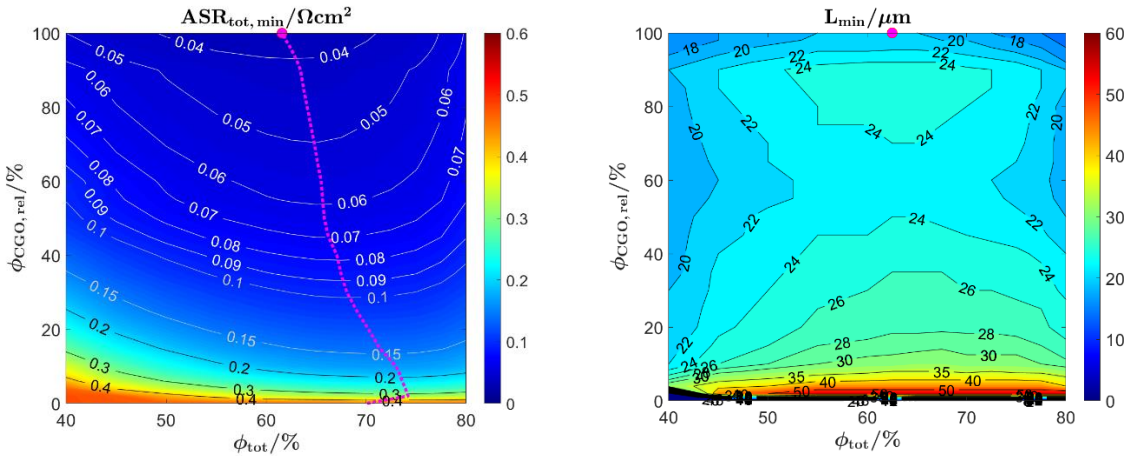

a) $ASR_{\text{tot,min}}$ b) L_{min}

Fig. 11: Minimal anode ASR $ASR_{\text{tot,min}}$ a) for the optimal AFL-thickness L_{min} b) as a function of the total solid volume fraction ϕ_{tot} and the composition $\phi_{\text{CGO,rel}}$, for $OCV_{\text{ref}} = 1050\text{mV}$ (water content 7 %) and $J = 0.208\text{A/cm}^2$ (i.e., the ASR is minimized by computing the optimum anode layer thickness at each point in the variation matrix). The dashed line represents the minimal ASR-value for a given composition and the magenta point indicates the global minimum. The color range (0 - 0.6 Wcm^2) for the ASR-plot in a) is the same as in Fig. 10 d) with constant AFL-thickness.

The optimal thickness of the anode functional layer (AFL) obviously changes for varying porosity and composition. Thus, the AFL-thickness is varied for every porosity-composition combination and the optimal AFL-thickness L_{min} providing the lowest ASR $ASR_{\text{tot,min}}$ is determined. The minimal anode ASR $ASR_{\text{tot,min}}$ is reported in Fig. 11 a). The dashed magenta line represents the minimal $ASR_{\text{tot,min}}$ and optimal total solid volume fraction ϕ_{tot} upon a compositional variation. The corresponding optimal anode layer thickness L_{min} is reported in in Fig. 11 b). The optimal anode layer thickness for a volume specific composition and ϕ_{tot} is in the range of $L = 12 - 55\ \mu\text{m}$. A steep increase of L_{min} is observed for an LSCT-content above 90 % (i.e., $\phi_{\text{CGO,rel}} < 10\%$). The low volume specific pore-CGO interface area is therewith partially compensated by a larger AFL-thickness to limit the HOR-ASR. Moreover, there is a moderate increase of L_{min} towards a CGO-content of $\phi_{\text{CGO,rel}} = 90\%$ because of the increasing ionic conductivity. For $\phi_{\text{CGO,rel}} > 90\%$, L_{min} decreases because of the finer microstructure, resulting in a different trade-off due to the smaller pores (i.e., higher Knudsen diffusion resistance). The dependency of L_{min} on ϕ_{tot} is relatively week. Towards low ϕ_{tot}, L_{min} decreases to limit the

charge transport resistance and towards high ϕ_{tot}, $L_{\min}$ decreases to limit the gas transport resistance. These trends are well visible in Fig. 10 b) and c) for the corresponding ASR contributions.

The total anode ASR $ASR_{\text{tot,min}}$ values (Fig. 11 a)) reported for the minimal AFL-thickness $L_{\min}$ are noticeable smaller compared to the total anode ASR $ASR_{\text{tot,min}}$ reported for a fixed AFL-thickness of $L = 15\,\mu\text{m}$ shown in Fig. 10 d). However, the differences are relatively small for sufficiently high CGO-contents (i.e., $\phi_{\text{CGO,rel}} > 20\%$). Thus, the AFL-layer thickness needs to be chosen appropriately, but there is a high robustness, e.g., for varying fabrication parameters.

4.3 Variation of ASR due to different operating conditions

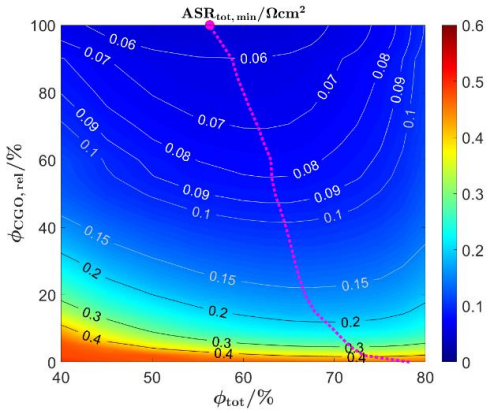

a) $ASR_{\text{tot,min}}$, water content 2.7 % and $J = 0.208\text{A/cm}^2$.

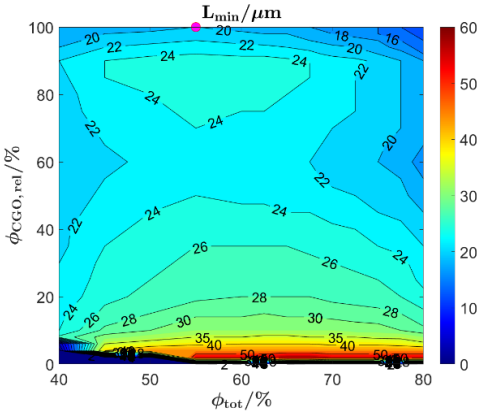

b) $L_{\min}$, water content 2.7 % and $J = 0.208\text{A/cm}^2$.

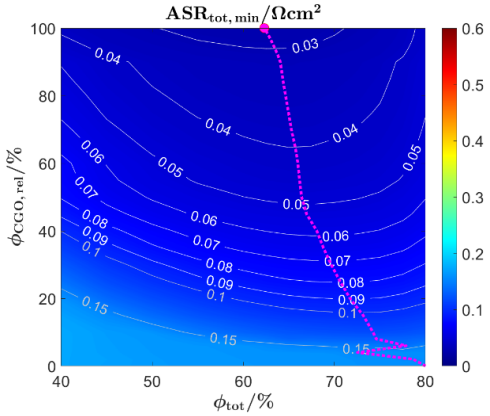

c) $ASR_{\text{tot,min}}$, water content 7 % and $J = 0.625\text{A/cm}^2$.

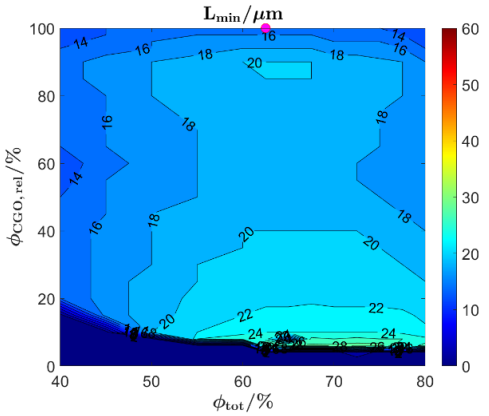

d) $L_{\min}$, water content 7 % and $J = 0.625\text{A/cm}^2$.

Fig. 12: Comparison of anode performances for two scenarios with different operating conditions. In both scenarios, the anode ASR $ASR_{\text{tot,min}}$ (left) is computed for the optimal AFL-thickness $L_{\min}$ (right) as a function of the total solid volume fraction ϕ_{tot} (x-axis) and the composition $\phi_{\text{CGO,rel}}$ (y-axis). a) and b) $OCV_{\text{ref}} = 1100\text{mV}$ (water content 2.7 %) and $J = 0.208\text{A/cm}^2$, c) and d) $OCV_{\text{ref}} = 1050\text{mV}$ (water content 7 %) and $J = 0.625\text{A/cm}^2$. The dashed line represents the minimal ASR-value for a given composition and the magenta point indicates the global minimum. The color ranges for ASR (0 - 0.6 Wcm^2) and thickness (0 – 60 mm) are the same as in Fig. 11 (reference operating conditions) for an easier comparison.

The anode model is calibrated for different operating conditions (see section 3.3) and thus, the effect of the operating conditions on the electrode design can be studied. Therefore, the minimal anode ASR $ASR_{\text{tot,min}}$ and the corresponding optimal AFL-thickness L_{min} as a function of composition and ϕ_{tot} are compared for two selected operating points (OP): OP1: $OCV_{\text{ref}} = 1100\text{mV}$ (water content 2.7 %) and $J = 0.208\text{A/cm}^2$ reported in Fig. 12 a) and b), and OP2: $OCV_{\text{ref}} = 1050\text{mV}$ (water content 7 %) and $J = 0.625\text{A/cm}^2$ reported in Fig. 12 c) and d). For OP2 with higher current density and water content, the anode ASR is considerably lower (by a factor of about two) than for OP1. Compared to the standard operating conditions ($OCV_{\text{ref}} = 1050\text{mV}$, water content 7 % and $J = 0.208\text{A/cm}^2$) reported in Fig. 11 a), the $ASR_{\text{tot,min}}$ is about 40 % higher for OP1 and about 25 % lower for OP2. Moreover, the optimal ϕ_{tot} is shifted to lower values for OP1 (around 4 vol. %) and to slightly larger values for OP2 (around 1 vol.%) compared to the standard operating conditions (Fig. 10 a)). For OP1, the optimal AFL-thickness L_{min} changes only marginally (Fig. 12 c)) compared to the standard operating conditions (Fig. 11 b)). For OP2, L_{min} changes more significantly (Fig. 12 d)) and is typically about $5\,\mu\text{m}$ lower. Moreover, L_{min} drops drastically around $\phi_{\text{CGO,rel}} < 10\%$. The large HOR resistance associated with the small active CGO- and LSCT-area for thin L is compensated by the small transport resistances due to gas and charge transport, which results to the lowest anode ASR for very low L. This behavior is also observable (but less clearly visible) for the other cases reported in Fig. 11-13, but only for even lower CGO-contents.

The operating conditions have a significant impact on the optimal ϕ_{tot} and AFL-thickness and thus it is advisable to check the anode design for all the important operating points. However, the change of the anode ASR upon a deviation from the optimal AFL-thickness is rather low, at least in the vicinity of an optimal design point. Thus, robust design parameters, which are insensitive to a change in the operating conditions and variations of the fabrication process are easily achievable with the presented approach.

4.4 Effect of a scaling of the microstructure

The influence of the characteristic structure size (i.e., varying the particle and pore sizes) on the anode performance shall be illustrated by a scaling of the microstructure. In Fig. 13, the total anode ASR $ASR_{\text{tot,min}}$ is reported together with the corresponding optimal AFL-thickness L_{min} for a scaling factor of 0.2 (a) and b)) and for a scaling factor of 5 (c) and d)). Thus, the characteristic structure sizes differ by a factor of 25 for these two datasets. The global optimum of the performance for the fine structure (scaling factor 0.2) is by a factor of about 3 lower compared to the coarse structure (scaling factor 5) and by a factor of about 1.6 lower compared to the unscaled structure reported in Fig. 11 a). The optimal ϕ_{tot} as a function of the composition is shifted to lower values (around 8 vol.%) for the fine structure, as the gas transport is more restricted because of the lower Knudsen diffusivity (associated with the smaller pores) and the charge transport is less restrictive because of the small AFL-thickness. A vice versa behavior can be observed for the coarse structure, where the optimal ϕ_{tot} is shifted to higher values for about 6 vol. %. Moreover, the increase of the anode ASR for decreasing CGO-content is much steeper for the coarse structure compared to the fine structure. This is predominantly because of the larger HOR resistance associated with the smaller volume specific surface area of the coarser microstructure.

For the fine structure, the optimal AFL-thickness L_{min} reported in Fig. 13 c) is typically around $L_{\text{min}} \approx 6\,\mu\text{m}$ and therewith about four times lower than for the unscaled structure (11 b)) with a typical $L_{\text{min}} \approx 23\,\mu\text{m}$. In contrast, for the coarse structure, the optimal AFL-thickness L_{min} reported in Fig. 13 d) is typically around $L_{\text{min}} \approx 70\,\mu\text{m}$, which is about three times higher compared to the unscaled structure (Fig. 11 b)). This behavior

can be explained by the extension of the reaction zone. For the coarse structure with low volume specific pore-CGO interface area, there is a larger extension of the reaction zone in order to achieve more available reaction sites. The associated decrease in the HOR-resistance thereby exceeds the additional resistance due to charge and gas transport. Consequently, the optimal AFL-thickness is considerably larger for coarser microstructures.

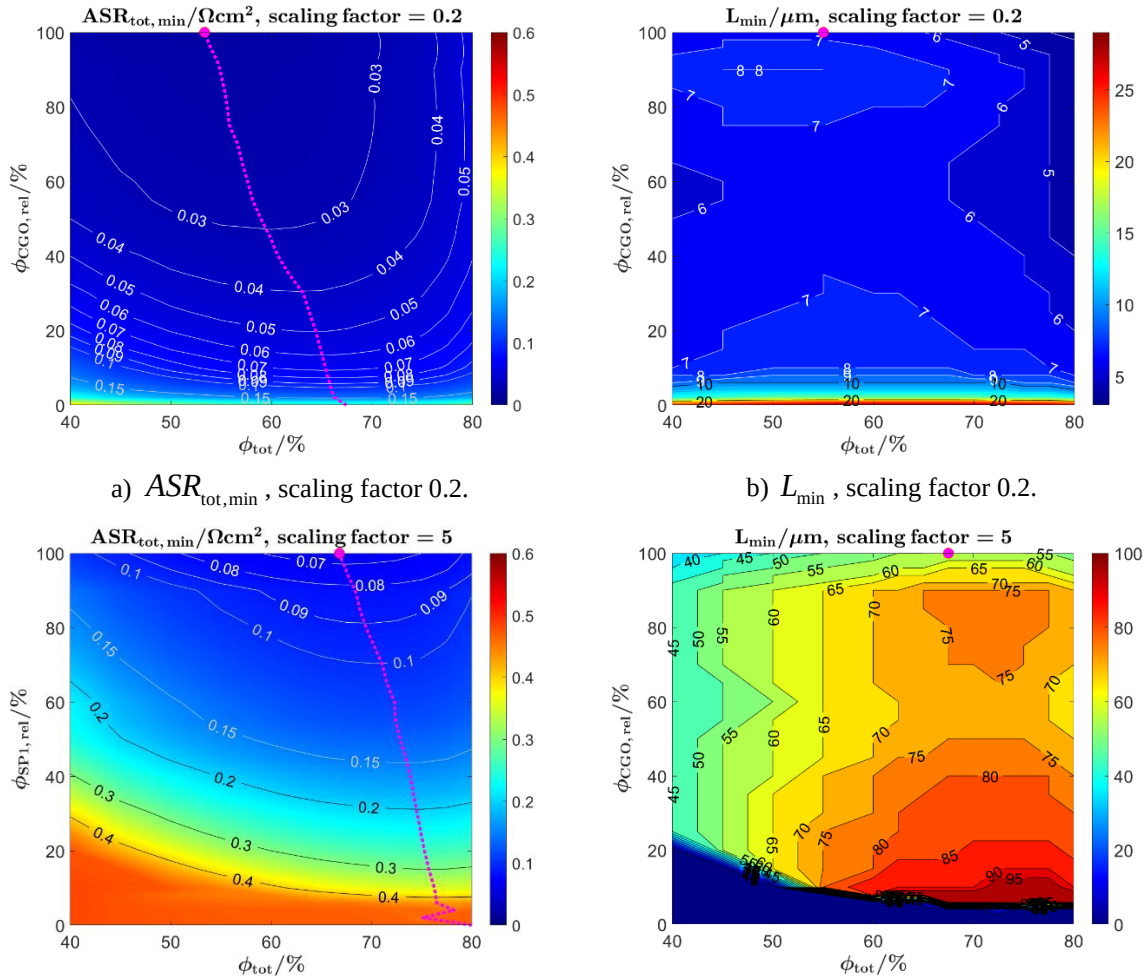

a) $ASR_{\mathrm{tot,min}}$, scaling factor 0.2.

b) L_{min}, scaling factor 0.2.

c) $ASR_{\mathrm{tot,min}}$, scaling factor 5

d) L_{min}, scaling factor 5.

Fig. 13: Impact of microstructure-scaling on electrode performance: anode ASR $ASR_{\mathrm{tot,min}}$ (left) for the optimal AFL-thickness L_{min} (right) is plotted as a function of the total solid volume fraction ϕ_{tot} and the composition $\phi_{\mathrm{CGO,rel}}$. Compared to the standard microstructure scenario (used in Figs. 10-12), a different scaling is perfromed in Fig. 13 a) and b) by a factor of 0.2 (i.e., finer microstructure), and in Fig. 13 c) and d) by a factor of 5 (i.e., coarser microstructure). The dashed line represents the minimal ASR-value for a given composition and the magenta point indicates the global minimum. The color ranges for the ASR-plots (0 - 0.6 $\mathrm{Wcm^2}$) in Figs. 13 a) and c) are the same as in Fig. 11 a) with the unscaled structure. The color ranges for the L_{min}-plots in Figs. 13 b) and d) are alligned to the reported values (i.e., they are different in Fig. 11 b)).

The observed trends are in good agreement with findings from the literature. An experimental study for the influence of the particle-size on the anode performance has e.g., been reported by. Sciazko et al. [43] for Ni-CGO anodes. As expected, the smallest CGO-particles resulted in the best initial performance. However, also the most severe degradation was observed for the smallest CGO-particles. Graves et al. [12] and Nenning et al. [13] reported a very low polarization resistance with pure nano-sized CGO-anodes, which verifies that a considerable reduction of the anode ASR can be achieved with a reduction of the particle size. The pure CGO anodes of Nenning et al. [13] were fabricated by a standard powder-based processing route and an AFL-thickness of only

$L = 3\,\mu m$ was used, which confirms the reported tendency of this work for lower optimal AFL-thicknesses for smaller structure sizes. On the other hand, Nakamura et al. [44] reported for an AFL-thickness variation of $L = [7, 20, 45]\,\mu m$ for a pure CGO anode with a relatively coarse microstructure in the micrometer range the best performance for the largest AFL-thickness of $L = 45\,\mu m$. This confirms a considerably larger optimal AFL-thickness for coarse microstructures.

5. CONCLUSION

A novel LSCT-CGO composite anode has been studied with a model-based approach. This Nickel-free composite anode does not suffer the degradation mechanism associated with Nickel-based electrodes. CGO provides a high ionic conductivity and a high electrochemical activity, which are both crucial for a high electrode performance. Moreover, the LSCT-perovskite provides a structural stabilization effect and thus an improved degradation behavior compared to pure CGO electrodes [1]. In addition, the LSCT introduces an improved current collection functionality because of its high intrinsic electronic conductivity.

In order to develop and optimize these LSCT-CGO anodes in a systematic and efficient way, Digital Materials Design (DMD) methodologies are employed. Thereby, DMD methodologies introduced in previous publications [22],[20] were applied for the virtual but realistic microstructure variation of LSCT-CGO anodes with respect to the LSCT-CGO composition and porosity. Furthermore, while exploring for optimum electrode performance (i.e., minimal ASR), the impacts from variations of particle and pore sizes (called scaling), electrode thickness and gas composition (water content) are also investigated. To model the impact of all these parameters, the DMD methodologies had to be complemented with a dedicated electrode model. For this purpose, a multiphysics continuum simulation model was developed and applied in this paper to predict the impact of the microstructure variation on the electrode performance, using the previously determined microstructure properties (i.e., relative ionic and electronic composite conductivity, 4 parameters for the parametrization of the dusty gas model and the volume specific pore-CGO and pore-LSCT interface areas) as an input.

The multiphysics electrode model is a key-element of the DMD-workflow as it resolves the trade-off between the different physical and microstructural aspects in a quantitative way. For example, the variation of porosity reveals that a high solid-phase volume fraction provides a high ionic and electronic conductivity, but the resulting low porosity hinders the gas transport and leads to a reduction of the volume specific surface area, which is available for the fuel oxidation reaction to take place. The multiphysics electrode model thereby allows to predict the optimal porosity for the lowest ASR for a specific LSCT-CGO composition. Typically, a minimum ASR is reached for optimized anode microstructures with 35% porosity and high CGO contents > 60%. These optimal parameters vary slightly with electrode thickness and gas composition. However, the simulation results also show, that the optimum design of the LSCT-CGO composite is very robust. This means, for example, that a deviation from the optimal porosity in a quite substantial range of $\varepsilon = 30\,\% - 40\,\%$ only leads to a moderate increase of the ASR of less than 4 %. In a similar way, good total anode ASR values are obtained for a large range of compositional variation. For example, the ASR only increases more than 50 % compared to the very low value of 100 % CGO when the LSCT-content exceeds 40 vol.%. This robustness allows to account for additional design goals like the degradation behavior (i.e., ensuring not only a good initial but also good long-term performance) and current collection functionality, e.g., with compositions containing ca. 20-40 vol.% LSCT. With our DMD-approach we can easily and efficiently explore the impact of additional design parameters such as a variation of the cell architecture, e.g., the electrode thickness. In fact, the optimal electrode thickness depends on the microstructure and material system. Especially, the optimal layer thickness increases towards low CGO-contents to enhance the otherwise small pore-CGO interface area relevant for the reaction kinetics (i.e., optimum thickness varies from 20 μm for 100% CGO to 32 μm for 10 % CGO for a fixed porosity of 35 %). However, the optimal electrode thickness varies only slightly for a large area in the design space (i.e., varying composition and porosity) and it is around 15-24 μm for a CGO content above 50 vol.%. Thereby also the dependency on the porosity is moderate. Thus, DMD results indicate that the layer thickness is again a robust design parameter.

In addition, the reaction kinetic of the model were calibrated to the experimental performance characterizations of the cells (i.e., EIS results) for different operating conditions. Hence, the impact of different operating conditions

on the cell performance and design parameters could be assessed. Thereby, it is found that the operating conditions have a significant impact on design parameters such as porosity and electrode layer thickness but are still small enough to allow for a robust design. Moreover, the effect of the characteristic particle and pore sizes can be easily assessed by the model. Thereby, it is clearly visible that the porosity and electrode layer thickness for a minimal ASR depend strongly on the structure size. This illustrates that an isolated optimization of a single design parameter does not lead to meaningful results. In contrast, the presented DMD framework, which combines stochastic microstructure simulations with a multiphysics electrode model, provides unique opportunities for efficient optimization in a multi-dimensional design space.

It must be emphasized that the presented simulation results are just a starting point for the huge playground of possible optimization routes, which might be explored based on the presented methods. Moreover, the presented DMD approach is applicable in a much larger context beyond its application to nickel-free SOFC anodes. First of all, it can be used for any other material system of electrodes in SOFC / SOEC applications. Moreover, the methods for microstructure optimization can easily be adapted to other energy applications like proton-exchange membrane fuel / electrolysis cells, Li-ion batteries, flow batteries and partially even for porous media in general (e.g., filters, sensors, membranes etc.).

ACKNOWLEDGEMENTS

This publication is based mainly on two research projects that received financial support from the Swiss Federal Office of Energy (SFOE, grant SI/501792-01 - 8100076) and from Eurostars (grant E!115455), which are gratefully acknowledged. A special thank is dedicated to Math2Market GmbH for the excellent collaboration in the Eurostars project, where a part of the applied DMD-methodologies was developed.

REFERENCES

1. Sciazko A, Komatsu Y, Yokoi R, Shimura T, Shikazono N. Effects of mass fraction of La0.9Sr0.1Cr0.5Mn0.5O3-δ and Gd0.1Ce0.9O2-δ composite anodes for nickel free solid oxide fuel cells. J Eur Ceram Soc [Internet]. 2022;42(4):1556–67. Available from: https://doi.org/10.1016/j.jeurceramsoc.2021.11.039
2. Khan MS, Lee SB, Song RH, Lee JW, Lim TH, Park SJ. Fundamental mechanisms involved in the degradation of nickel–yttria stabilized zirconia (Ni–YSZ) anode during solid oxide fuel cells operation: A review. Ceram Int [Internet]. 2016;42(1):35–48. Available from: http://dx.doi.org/10.1016/j.ceramint.2015.09.006
3. Holzer L, Iwanschitz B, Hocker T, Münch B, Prestat M, Wiedenmann D, et al. Microstructure degradation of cermet anodes for solid oxide fuel cells: Quantification of nickel grain growth in dry and in humid atmospheres. J Power Sources [Internet]. 2011;196(3):1279–94. Available from: http://dx.doi.org/10.1016/j.jpowsour.2010.08.017
4. He H, Hill JM. Carbon deposition on Ni/YSZ composites exposed to humidified methane. Appl Catal A Gen. 2007;317(2):284–92.
5. Brus G, Nowak R, Szmyd JS, Komatsu Y, Kimijima S. An experimental and theoretical approach for the carbon deposition problem during steam reforming of model biogas. J Theor Appl Mech. 2015;53(2):273–84.
6. Yu F, Xiao J, Zhang Y, Cai W, Xie Y, Yang N, et al. New insights into carbon deposition mechanism of nickel/yttrium-stabilized zirconia cermet from methane by in situ investigation. Appl Energy [Internet]. 2019;256. Available from: https://doi.org/10.1016/j.apenergy.2019.113910
7. Matsuzaki Y, Yasuda I. Poisoning effect of sulfur-containing impurity gas on a SOFC anode: Part I. Dependence on temperature, time, and impurity concentration. Solid State Ionics. 2000;132(3):261–9.
8. Fouquet D, Müller AC, Weber A, Ivers-Tiffée E. Kinetics of oxidation and reduction of Ni/YSZ cermets. Ionics (Kiel). 2003;9(1–2):103–8.
9. Shu L, Sunarso J, Hashim SS, Mao J, Zhou W, Liang F. Advanced perovskite anodes for solid oxide fuel cells: A review. Int J Hydrogen Energy [Internet]. 2019;44(59):31275–304. Available from: https://doi.org/10.1016/j.ijhydene.2019.09.220
10. Burnat D, Nasdaurk G, Holzer L, Kopecki M, Heel A. Lanthanum doped strontium titanate - ceria anodes: deconvolution of impedance spectra and relationship with composition and microstructure. J Power Sources [Internet]. 2018;385(February):62–75. Available from: https://doi.org/10.1016/j.jpowsour.2018.03.024
11. Price R, Cassidy M, Grolig JG, Mai A, Irvine JTS. Preparation and Testing of Metal/Ce 0.80 Gd 0.20 O 1.90 (Metal: Ni, Pd, Pt, Rh, Ru) Co-Impregnated La 0.20 Sr 0.25 Ca 0.45 TiO 3 Anode Microstructures for Solid Oxide Fuel Cells. J Electrochem Soc. 2019;166(4):F343–9.
12. Graves C, Martinez L, Sudireddy BR. High Performance Nano-Ceria Electrodes for Solid Oxide Cells. ECS Trans. 2016;72(7):183–92.

13. Nenning A, Holzmann M, Fleig J, Opitz AK. Excellent kinetics of single-phase Gd-doped ceria fuel electrodes in solid oxide cells. Mater Adv. 2021;2(16):5422–31.
14. Savaniu CD, Irvine JTS. La-doped SrTiO3 as anode material for IT-SOFC. Solid State Ionics. 2011;192(1):491–3.
15. Verbraeken MC, Iwanschitz B, Mai A, Irvine JTS. Evaluation of Ca Doped La 0.2 Sr 0.7 TiO 3 as an Alternative Material for Use in SOFC Anodes. J Electrochem Soc. 2012;159(11):F757–62.
16. Ramos T, Veltzé S, Sudireddy BR, Jørgensen PS, Theil Kuhn L, Holtappels P. Effect of Ru/CGO versus Ni/CGO co-infiltration on the performance and stability of STN-based SOFCs. Fuel Cells. 2014;14(6):1062–5.
17. Price R, Weissen U, Grolig JG, Cassidy M, Mai A, Irvine JTS. Durability of La0.20Sr0.25Ca0.45TiO3-based SOFC anodes: identifying sources of degradation in Ni and Pt/ceria co-impregnated fuel electrode microstructures. J Mater Chem A [Internet]. 2021;9(16):10404–18. Available from: http://dx.doi.org/10.1039/D1TA00416F
18. Futamura S, Muramoto A, Tachikawa Y, Matsuda J, Lyth SM, Shiratori Y, et al. SOFC anodes impregnated with noble metal catalyst nanoparticles for high fuel utilization. Int J Hydrogen Energy [Internet]. 2019;44(16):8502–18. Available from: https://doi.org/10.1016/j.ijhydene.2019.01.223
19. Marmet P. Digital Materials Design of Solid Oxide Fuel Cell Anodes [Internet]. University of Fribourg, Switzerland, URL: https://doi.org/10.21256/zhaw-28430; 2023. Available from: https://doi.org/10.21256/zhaw-28430
20. Marmet P, Holzer L, Hocker T, Muser V, Boiger GK, Fingerle M, et al. Stochastic microstructure modeling of SOC electrodes based on a pluri-Gaussian method. Energy Adv [Internet]. 2023;2(11):1942–67. Available from: https://doi.org/10.1039/D3YA00332A
21. Marmet P, Holzer L, Hocker T, Muser V, Boiger GK, Fingerle M, et al. Python app for stochastic microstructure modeling of SOC electrodes based on a pluri-Gaussian method. Zenodo [Internet]. 2023; Available from: https://doi.org/10.5281/zenodo.7744110
22. Marmet P, Holzer L, Hocker T, Boiger GK, Bausinger H, Mai A, et al. Standardized microstructure characterization of SOC electrodes as a key element for Digital Materials Design. Energy Adv. 2023;2(7):980–1013.
23. Marmet P, Holzer L, Hocker T, Boiger GK, Bausinger H, Mai A, et al. Characterization-app: Standardized microstructure characterization of SOC electrodes as a key element for Digital Materials Design [Internet]. Zenodo; 2023. Available from: https://doi.org/10.5281/zenodo.7741305
24. Krishna R, Wesselingh JA. The Maxwell-Stefan approach to mass transfer. Chem Eng Sci. 1997;52(6):861–911.
25. Liu S, Kong W, Lin Z. Three-dimensional modeling of planar solid oxide fuel cells and the rib design optimization. J Power Sources. 2009;194(2):854–63.
26. Bertei A, Nicolella C. Common inconsistencies in modeling gas transport in porous electrodes: The dusty-gas model and the Fick law. J Power Sources [Internet]. 2015;279:133–7. Available from: http://dx.doi.org/10.1016/j.jpowsour.2015.01.007
27. Kishimoto M, Lomberg M, Ruiz-Trejo E, Brandon NP. Numerical modeling of nickel-infiltrated gadolinium-doped ceria electrodes reconstructed with focused ion beam tomography. Electrochim Acta [Internet]. 2016;190:178–85. Available from: http://dx.doi.org/10.1016/j.electacta.2015.12.044
28. Marmet P, Holzer L, Grolig JG, Bausinger H, Mai A, Brader JM, et al. Modeling the impedance response and steady state behaviour of porous CGO-based MIEC anodes. Phys Chem Chem Phys. 2021;23(40):23042–74.
29. Price R, Cassidy M, Schuler JA, Mai A, Irvine JTS. Development and Testing of Impregnated La 0.20 Sr 0.25 Ca 0.45 TiO 3 Anode Microstructures for Solid Oxide Fuel Cells. ECS Trans. 2017;78(1385).
30. Price R, Cassidy M, Schuler JA, Mai A, Irvine JTS. Screen Printed Porous La 0.20 Sr 0.25 Ca 0.45 TiO 3 Fuel Electrode Scaffold Microstructures: Optimisation of Interaction with Impregnated Catalysts for More Durable Performance. ECS Trans. 2015;68(1499).
31. Burnat D, Kontic R, Holzer L, Steiger P, Ferri D, Heel A. Smart material concept: Reversible microstructural self-regeneration for catalytic applications. J Mater Chem A. 2016;4(30):11939–48.
32. Holzer L, Marmet P, Fingerle M, Wiegmann A, Neumann M, Schmidt V. Tortuosity and microstructure effects in porous media: classical theories, empirical data and modern methods [Internet]. 1st ed. Springer Cham, ISBN: 978-3-031-30477-4; 2023. Available from: https://link.springer.com/book/10.1007/978-3-031-30477-4
33. GeoDict simulation software Release 2023 (Revision 61624), by Math2Market GmbH, Germany, DOI: 10.30423/release.geodict2023.
34. Kaleidosim Technologies AG. Kaleidosim-Cloud [Internet]. Zurich; 2022. Available from: https://kaleidosim.com
35. Dierickx S, Joos J, Weber A, Ivers-Tiffée E. Advanced impedance modelling of Ni/8YSZ cermet anodes. Electrochim Acta. 2018;265:736–50.
36. Monaco F, Effori E, Hubert M, Siebert E, Geneste G, Morel B, et al. Electrode kinetics of porous Ni-3YSZ cermet operated in fuel cell and electrolysis modes for solid oxide cell application. Electrochim Acta [Internet]. 2021;389(138765). Available from: https://doi.org/10.1016/j.electacta.2021.138765
37. COMSOL AB. COMSOL Multiphysics® V. 5.5 [Internet]. Stockholm, Sweden: COMSOL AB, Stockholm, Sweden; 2019. Available from: www.comsol.com

38. Fuller EN, Schettler PD, Giddings JC. A new method for prediction of binary gas-phase diffusion coefficients. Ind Eng Chem. 1966;58(5):18–27.
39. Becker J, Wieser C, Fell S, Steiner K. A multi-scale approach to material modeling of fuel cell diffusion media. Int J Heat Mass Transf. 2011;54(7–8):1360–8.
40. Zhou X, Yan N, Chuang KT, Luo J. Progress in La-doped SrTiO3 (LST)-based anode materials for solid oxide fuel cells. RSC Adv. 2014;4(1):118–31.
41. Steele BCH. Appraisal of Ce1-yGdyO2-y/2 electrolytes for IT-SOFC operation at 500. Solid State Ionics. 2000;129(1):95–110.
42. Todd B, Young JB. Thermodynamic and transport properties of gases for use in solid oxide fuel cell modelling. J Power Sources. 2002;110(1):186–200.
43. Sciazko A, Miyahara K, Komatsu Y, Shimura T, Jiao Z, Shikazono N. Influence of Initial Powder Morphology on Polarization Characteristics of Nickel/Gadolinium-Doped-Ceria Solid Oxide Fuel Cells Electrode. J Electrochem Soc. 2019;166(2):F44–52.
44. Nakamura T, Yashiro K, Kaimai A, Otake T, Sato K, Kawada T, et al. Determination of the Reaction Zone in Gadolinia-Doped Ceria Anode for Solid Oxide Fuel Cell. J Electrochem Soc. 2008;155(12):B1244–50.